Lithospheric modification at the onset of the destruction of the North China Craton: evidence from Late Triassic mafic dykes

Chao Wang[a,b,c]*, Shuguang Song[b]*, Li Su[d], Mark B. Allen[e], Jinlong Dong[b]

[a] *School of Earth Sciences and Resources, China University of Geosciences, Beijing 100083, China*

[b] *MOE Key Laboratory of Orogenic Belts and Crustal Evolution, School of Earth and Space Sciences, Peking University, Beijing 100871, China*

[c] *Department of Earth Sciences, The University of Hong Kong, Pokfulam Road, Hong Kong, China*

[d] *School of Scientific Research and State Key Laboratory of Geological Processes and Mineral Resources, China University of Geosciences, Beijing 100083, China*

[e] *Department of Earth Sciences, Durham University, Durham DH1 3LE, UK*

Revised manuscript for *Chemical Geology*

*corresponding authors

Chao Wang (daniel.wangchao@gmail.com; chao.wang@cugb.edu.cn)

Shuguang Song (sgsong@pku.edu.cn)

Abstract

Mantle-derived magmatism provides important insights for understanding the mechanism of lithospheric thinning. Here we report the results of an integrated geochronological and geochemical study of Late Triassic mafic dykes in Eastern Hebei, northern North China Craton. *In situ* zircon U-Pb dating shows that the dykes were emplaced between 238 and 223 Ma; the coeval Gaojiadian and Mataizi dykes intruded Precambrian basement at 238–234 Ma and the Saheqiao dyke was emplaced into Neoarchean supracrustal rocks later at 223 ± 4 Ma (2*s*). Bulk-rock geochemistry indicates that the Late Triassic dykes in Eastern Hebei were produced by melting of ancient lithospheric mantle within the garnet-spinel transition zone (~70–80 km), heated by upwelling asthenosphere. This ancient lithospheric mantle had been metasomatized during previous subduction events. The Gaojiadian and Mataizi dykes resulted from higher degrees of partial melting at slightly lower pressures than the Saheqiao dyke. The melting depth of Late Triassic dykes in Eastern Hebei indicates that the intact ancient lithospheric mantle had been at least locally modified/thinned to ~70–80 km by the Late Triassic. The intrusion of these Late Triassic dykes took place at the onset of the lithospheric thinning of the North China Craton, caused by post-collisional extension after subduction and collision of neighboring blocks with the North China Craton.

Keywords: Mafic dykes; Lithospheric modification; Destruction or lithospheric thinning; North China Craton

1 Introduction

The North China Craton (NCC) is unique compared with other Archean cratons in that its lithosphere underwent significant thinning during the Mesozoic; this event has been extensively and intensively studied for several decades (e.g., Gao et al., 2004; Liu et al., 2019; Wu et al., 2019; Xu, 2001; Yang and Wu, 2009; Yang et al., 2008; Zhu and Xu, 2019). The thick and cold ancient lithospheric mantle present underneath the NCC in the Paleozoic had been converted into a thin and hot lithospheric mantle, as sampled by mantle xenoliths in Paleozoic kimberlites and Cenozoic basalts (Gao et al., 2002; Wu et al., 2006; Xu, 2001; Xu et al., 2009; Zhang et al., 2008a). The Mesozoic lithospheric thinning of the NCC resulted in widespread magmatism (Yang et al., 2008; Zhang et al., 2014), accompanied by intensive deformation (Wang et al., 2018; Zhang et al., 2014) and mineralization (Li and Santosh, 2017; Yang and Santosh, 2020). Although the Late Mesozoic is the most important stage for the lithospheric thinning of the NCC (Wu et al., 2005, 2019; Yang and Wu, 2009; Yang et al., 2008; Zhu and Xu, 2019), it is generally acknowledged that lithospheric thinning of the NCC initiated at its margins in the Late Triassic, and afterwards spread diachronously across the NCC (Wang et al., 2015; Yang et al., 2008, 2010; Zhang et al., 2014).

The first-order cause of the destruction or lithospheric thinning of the NCC is believed to be interaction between the NCC and neighboring blocks, including the Yangtze Craton to the south, the Paleo-Asian plate and the Siberian plate to the north, and the Paleo-Pacific plate to the east (Meng et al., 2020; Wang et al., 2015, 2017; Wu et al., 2019; Yang and Wu, 2009; Zhang et al., 2014). However, the detailed mechanisms of the processes involved are still under debate, and various mechanisms have been proposed in previous research (e.g., Wu et al., 2006, 2019; Xu et al., 2009; Yang and Wu, 2009; Yang et al., 2008; Zhang et al., 2014; Zhu and Xu, 2019). These include thermo-mechanical and chemical erosion from below (Xu, 2001), delamination/foundering (Gao et al., 2004), peridotite-melt interaction (Zhang et al., 2008a), extension (Liu et al., 2008), basal hydration weakening (Niu, 2005, 2014) or removal of lithospheric mantle induced by lithospheric folding (Zhang, 2012).

Magmatism, especially mantle-derived magmatic rocks, can probe the geodynamic processes responsible for the lithospheric thinning of the NCC, as compositions and ages of these rocks potentially record the source characteristics and melting conditions of the lithosphere and/or asthenosphere involved, as well as the timing and emplacement mechanism(s) (e.g., Liu et al., 2018; Ma et al., 2014a, 2014b, 2016; Niu et al., 2017; Wan et al., 2019; Wang et al., 2020; Xue et al., 2019). The thermal and chemical state of the overlying lithosphere can be affected and modified by the addition of volatiles released from previously subducted slabs (Niu, 2005) and the upwelling convective asthenosphere (Xu et al., 2009). Therefore, it is crucial to understand how any slab-derived volatiles and juvenile, depleted, asthenospheric mantle participated and interacted with other source components during the lithospheric thinning of the NCC, particularly at its initial stage. Recent investigations revealed that Late Triassic mantle-derived magmatic rocks in the NCC were predominantly sourced from a subduction-modified ancient lithospheric mantle, with a contribution from the juvenile asthenospheric mantle (e.g., Chen et al., 2008; Li et al., 2020; Niu et al., 2012, 2017; Yang et al., 2012). But, due to the scarcity of Late Triassic mantle-derived rocks in the NCC (Zhang et al., 2014), the nature and the thickness of the ancient lithospheric mantle during the Late Triassic are not clear.

In this contribution, we present an integrated study involving *in situ* zircon U-Pb dating, mineral chemistry, bulk-rock elemental and Sr-Nd isotope geochemistry for Late Triassic (238–223 Ma) mafic dykes in Eastern Hebei of the northern NCC (Fig. 1), to better understand the properties of its ancient lithospheric mantle root at the onset of lithospheric thinning of the NCC. We demonstrate that these dykes were derived from a modified ancient lithospheric mantle, and that the thickness of the intact ancient lithosphere beneath the NCC had been locally reduced to ~70–80 km by the Late Triassic, as the result of previously subduction-related metasomatism.

2 Geological background and samples

The NCC is bounded by several orogenic belts, including the late Paleozoic Central Asian Orogenic Belt (CAOB) to the north, the Triassic Qinling-Dabie Orogen to the south and the Sulu Orogen to the east, and is cut by the Tan-Lu strike-slip fault in the east (Fig. 1a). As the largest and oldest cratonic block in China, the NCC preserves vestiges of Eoarchean crustal records older than 3.8 Ga (Liu et al., 1992). The NCC was preliminarily cratonized through amalgamation of micro-continents at the end of the Neoarchean (e.g., Wang et al., 2016), and it was finally sutured along three major orogenic belts in the Paleoproterozoic (Santosh et al., 2007; Tam et al., 2011; Zhao et al., 2005). After the final cratonization in the Paleoproterozoic, the NCC remained tectonically stable and developed a thick sedimentary cover until the end of the Paleozoic, with scattered and episodic Proterozoic mantle plume-related magmatic rocks (e.g., Peng et al., 2012; Zhang et al., 2017). In the Paleozoic, a thick cratonic lithosphere existed beneath the NCC, as evidenced by the Paleozoic diamondiferous kimberlites in the eastern NCC (Zhang et al., 2010). However, the lithosphere of the NCC began to experience significant thinning in the Mesozoic, with intensive magmatism, deformation and mineralization widely distributed across the eastern NCC (Yang and Wu, 2009; Yang et al., 2003; Zhang et al., 2014). Comprehensive geochronological investigations reveal that Mesozoic magmatism in the eastern NCC occurred in three major pulses: the Late Triassic (230–210 Ma), the Jurassic (180–153 Ma) and the Early Cretaceous (135–110 Ma) (Wang et al., 2015, 2017; Wu et al., 2005; Yang and Wu, 2009; Zhang et al., 2014). Late Triassic magmatism is volumetrically minor compared to its Jurassic and Early Cretaceous counterparts, including some sporadically distributed mafic dykes, intermediate-felsic rocks, alkaline intrusives and ultramafic-mafic complexes in the northern NCC (Wang et al., 2015; Jia et al., 2019; Li et al., 2020; Yang et al., 2004; Zhang et al., 2012, 2014).

The study area is located in Eastern Hebei, which lies west of the Tan-Lu fault and in the eastern segment of the northern part of the NCC (Fig. 1a). Precambrian basement in Eastern Hebei mainly consists of Neoarchean tonalite-trondhjemite-granodioirte (TTG) gneisses, charnockites, and supracrustal rocks metamorphosed to various degrees (Duan et al., 2017; Liou and Guo, 2019; Yang and Wei, 2017a, 2017b), with a few Paleo-Mesoarchean supracrustal remnants (detrital zircons or dismembered enriched plume-related volcanic successions) (Liu et al., 1992; Liou et al., 2020; Nutman et al., 2011; Wang et al., 2019) and Paleoproterozoic metamorphosed mafic dykes (Duan et al., 2015; Yang and Wei, 2017a). Paleoproterozoic to Mesozoic sedimentary cover was deposited uncomformably over the Precambrian basement, with a few discrete volcanic layers within the sequence. The Precambrian basement was also intruded by Mesozoic felsic plutons and mafic dykes (Fan et al., 2017; Xiong et al., 2018). These dykes are widespread albeit thinly-distributed and dyke lengths are on the scale of 1–4 km (Fig. 1c and d). However, ages and petrogenesis of these Mesozoic mafic dykes remain unresolved as no comprehensive investigations have previously been carried out.

The studied mafic dyke samples were collected to the north of Santunying and to the south of Lulong, in the central-east part of Eastern Hebei (Fig. 1b). Different portions of the mafic dykes were sampled when possible and samples were all collected from the interior of the dykes to reduce crustal contamination as much as possible. To the north of Santunying, the Neoarchean TTG gneisses host meta-supracrustal lenses that were intruded by Mesozoic mafic dykes and felsic plutons (Fig. 1c). The dykes show some lithological variations but have uniform NNE strikes. Two dykes near Gaojiadian and Saheqiao, north of Santunying, were selected as representative examples of this dyke suite for detailed study. Samples do not show significant mineralogical variations within each dyke. Both dykes intruded Neoarchean TTG gneisses with sharp contacts (Fig. 2a and c). The Gaojiadian samples are fresh and display typical ophitic textures with interstitial anhedral to subhedral clinopyroxene surrounded by euhedral lath-shaped plagioclase (Fig. 2b), with apatite, magnetite, titanite and zircon as accessory phases. The Saheqiao samples have a mineral assemblage of euhedral hornblende and anhedral to subhedral plagioclase with accessory apatite, magnetite, titanite and zircon, and experienced post-emplacement greenschist-facies alteration with some hornblende and almost all plagioclase metamorphosed to actinolite and albite (Fig. 2d). To the south of Lulong, widespread Neoarchean supracrustal gneisses were intruded by a suite of Mesozoic mafic dykes, and these dykes also show coherent NE strikes (Fig. 1d). One dyke near Mataizi was sampled for detailed study, as a representative example of this dyke suite to the south of Lulong (Fig. 2e). The Mataizi samples were strongly foliated and consist of hornblende, biotite and plagioclase (Fig. 2f). We also examined other outcrops of dykes in Eastern Hebei, but samples at these outcrops are either strongly weathered or yielded no zircons for U-Pb dating.

3 Analytical methods and results

Geochronological and geochemical data presented in this study include *in situ* zircon U-Pb isotopes, mineral chemistry, and bulk-rock geochemistry; the analytical methods are given in the Supplementary Material; all the data are presented in Tables S1–7.

3.1 *In situ* zircon U-Pb ages

Three representative samples of Mesozoic mafic dykes (sample J1416 for the Gaojiadian dyke, sample 15SHQ05 for the Saheqiao dyke and sample 18NC51 for the Mataizi dyke) were selected for *in situ* zircon U-Pb dating, and the data are listed in Tables S1–2 and plotted in Fig. 3. For samples J1416 and 15SHQ05, zircons are not abundant and only about 100 zircon grains were separated from each sample (~15 kg), but in rare cases zircons can be observed within magmatic minerals in thin sections (Fig. 2b and d). These zircons are mostly subhedral to euhedral, colorless and transparent crystals 100–150μm in length and showing straight and wide growth bands and patchy zoning typical of a magmatic origin, without any relic cores in cathodoluminescence images (Fig. 3a). Their morphological features are not consistent with a derivation of these zircons from felsic magmas (Corfu et al., 2003; Wan et al., 2011), which typically have oscillatory growth zoning. In addition, their tightly clustered age distributions (see below), and the rarity of contemporaneous Late Triassic magmatism in the study area also rule out the possibility that these zircons were xenocrysts captured during intrusion of their host mafic dykes. These dykes are composed of phaneritic Si-saturated minerals (Fig. 2b and d) with high Zr abundances (119 ppm for sample J1416 and 142 ppm for sample 15SHQ05; Table S6), making it possible that these zircons could have originally crystallized from the parental magmas of their host rocks. Therefore, the ages obtained from these zircons are interpreted as the crystallization ages of the mafic dykes. Zircons are also not abundant in the Mataizi dyke sample 18NC51, and only 68 zircon grains were extracted from this sample (~15 kg). However, most of the separated zircons from this sample are xenocrysts with euhedral–prismatic shape and oscillatory zoning (Fig. 3a), which could indicate that they were captured from the intruded Neoarchean supracrustal gneisses. Only a few of them are magmatic zircons showing similar morphological characteristics with those from the Gaojiadian and Saheqiao dyke samples, and the obtained ages from these magmatic zircons most likely represent the crystallization age of the Mataizi dyke.

Nineteen zircons from the Gaojiadian dyke sample J1416 were analyzed and yield a $^{206}Pb/^{238}U$ age range of 242 ± 4 to 227 ± 3 Ma (1*s*) and Th/U ratios of 0.62–1.37 (Table S1). These zircons are all concordant and give a concordia age of 234 ± 3 Ma (2*s*, mean square weighted deviation (MSWD) = 0.15) (Fig. 3b), which is in accordance with the weighted mean $^{206}Pb/^{238}U$ age of 234 ± 2 Ma (2*s*, MSWD = 1.13). Eleven zircons from the Saheqiao dyke sample 15SHQ05 were dated and show a narrow range of $^{206}Pb/^{238}U$ ages (231 ± 3 to 217 ± 3 Ma (1*s*); Table S1) with Th/U ratios generally > 0.4. These zircons are mostly concordant and yield a concordia age of 223 ± 4 Ma (2*s*, MSWD = 0.28) (Fig. 3c), which is consistent with the weighted mean $^{206}Pb/^{238}U$ age of 224 ± 2 Ma (2*s*, MSWD = 1.06). Thirteen zircons from the Mataizi dyke sample 18NC51 were analyzed and are all concordant (Fig. 3d). Eleven of these zircons are xenocrysts with Neoarchean $^{207}Pb/^{206}Pb$ ages of 2821 ± 18 to 2524 ± 19 Ma (1*s*) and Th/U ratios of 0.45–1.69 (Table S2). Two concordant magmatic zircons yield $^{206}Pb/^{238}U$ ages of 245 ± 5 and 233 ± 4 Ma (1*s*) and Th/U ratios of 0.53 and 0.18, with a weighted mean $^{206}Pb/^{238}U$ age of 238 ± 6 Ma (2*s*, MSWD = 3.5).

In summary, the Mesozoic mafic magmatism in Eastern Hebei took place in the Late Triassic (238–223 Ma). The Gaojiadian and Mataizi dykes were coeval and intruded the Precambrian basement at 238–234 Ma, which was slightly earlier than the Saheqiao dyke (223 Ma).

3.2 Mineral chemistry

Two representative samples for mafic dykes in the study area (sample J1416 for the Gaojiadian dyke and sample 15SHQ03 for the Saheqiao dyke) were selected for detailed mineral chemistry analyses. The Mataizi dyke samples were not chosen for mineral chemistry study as these strongly foliated samples have experienced post-magmatic alteration. Representative mineral compositions are listed in Tables S3–5 and plotted in Fig. 4.

Clinopyroxene in the Gaojiadian dyke sample J1416 contains 0.26–0.36 of wollastonite (= $Ca/(Fe^{2+} + Mg + Ca)$), 0.31–0.44 of enstatite (= $Mg/(Fe^{2+} + Mg + Ca)$), 0.16–0.30 of ferrosilite (= $Fe^{2+}/(Fe^{2+} + Mg + Ca)$), and 0.05–0.11 of jadeite (= Al^{VI}) + aegirine (= Fe^{3+}), classifying it as augite

(Table S3 and Fig. 4a). Plagioclase in the Gaojiadian dyke sample has no obvious zonation and is labradorite to andesine in composition, and has X_{An} [=Ca/(Ca + Na + K)] of 0.46–0.69 (Table S4 and Fig. 4b).

Magmatic hornblende crystals in the Saheqiao sample 15SHQ03 show similar compositions of Ca_B = 1.97–2.03, $(Na + K)_A$ = 0.69–0.90, Ti = 0.32–0.46, and Si = 5.72–5.85, and has X_{Mg} [$Mg/(Mg + Fe^{2+})$] ranging between 0.61–0.78 (Table S5), being pargasite (Fig. 4c). Plagioclase in the Saheqiao sample 15SHQ03 is almost purely albite in composition, with X_{Ab} [=Na/(Ca + Na + K)] ranging from 0.95 to 0.99, which is not a primary magmatic phase but the result of post-emplacement greenschist-facies alteration (Table S4).

3.3 Bulk-rock geochemistry

Five representative samples for the Gaojiadian dyke, four representative samples for the Mataizi dyke and four representative samples for the Saheqiao dyke were selected for bulk-rock major and trace element and Sr-Nd isotope analyses, and the data are listed in Tables S6–7.

The Gaojiadian dyke samples were collected from two outcrops of this dyke (Fig. 1c). They are mafic in composition with SiO_2 contents of 47.84–52.44 wt.% and plot in the 'basalt' field in Fig. 5a (Table S6). They are characterized by high contents of TiO_2 (1.63–2.85 wt.%) and Fe_2O_{3T} (14.02–16.64 wt.%), but are relatively low in MgO (4.44–6.00 wt.%), thus they have moderate Mg# of 38.5–43.7 and high FeO_T/MgO (Fig. 5b). They show moderate enrichment in light rare earth elements (LREEs) over heavy rare earth elements (HREEs) ($(La/Yb)_N$ = 2.5–8.8) with weak negative Eu anomalies (Eu/Eu* = 0.95–0.99), ranging between those of the enriched mid-ocean ridge basalt (E-MORB) and ocean island basalt (OIB) (Fig. 6a). In the primitive mantle (PM)-normalized trace element diagram (Fig. 6b), they have variable contents of large ion lithophile elements (LILEs; e.g., Rb, Ba and Th) and show various degrees of depletion in high-field strength elements (HFSEs; e.g., Nb, Ta, Zr and Hf) and negative anomalies of Sr. They also have relatively low abundances of compatible elements (Cr = 63–110 ppm and Ni = 61.0–90.1 ppm) (Table S6). These samples display a range of initial $^{87}Sr/^{86}Sr$ ratios of 0.707348–0.709471 and negative $\varepsilon_{Nd}(t)$ values of -15.5 to -7.7 with depleted mantle Nd model ages (T_{DM}) of 2259–1622 Ma, when calculated at 234 Ma (Table S7 and Fig. 7).

The Mataizi dyke samples have similar bulk-rock geochemical features to the Gaojiadian dyke samples. They are all mafic in compositions with SiO_2 contents of 46.48–50.09 wt.% and plot in the ‘basalt’ field in Fig. 5a (Table S6). They have high contents of TiO_2 (1.66–1.80 wt.%) and Fe_2O_{3T} (15.79–16.84 wt.%) but have low MgO contents (5.27–5.40 wt.%), and thus they have moderate Mg# of 38.8–39.9 and accordingly high FeO_T/MgO (Fig. 5b). They are moderately enriched in LREEs over HREEs ($(La/Yb)_N$ = 3.6–3.9) with weak negative Eu anomalies (Eu/Eu* = 0.90), also ranging between those of the E-MORB and OIB (Fig. 6a). In the PM-normalized trace element diagram (Fig. 6b), they have high contents of LILEs and show depletion in HFSEs. They also have relatively low abundances of compatible elements (Cr = 74–85 ppm and Ni = 52.3–56.6 ppm) (Table S6). These samples yield initial $^{87}Sr/^{86}Sr$ ratios of 0.706472–0.708661 and negative $\varepsilon_{Nd}(t)$ values of -11.1 to -10.7 with T_{DM} ages of 1902–1870 Ma, when calculated at 238 Ma (Table S7 and Fig. 7)

Compared with the Gaojiadian and Mataizi dyke samples, the Saheqiao dyke samples are also mafic in composition but have lower contents of SiO_2 (45.63–47.64 wt.%), and fall in the ‘alkali basalt’ field in Fig. 5a (Table S6). They have lower Fe_2O_{3T} (9.92–10.49 wt.%), but higher MgO (7.40–9.21 wt.%), Mg# (58.9–63.8) and compatible elements (Cr = 114–400 ppm and Ni = 79.1–156.4 ppm) and thus lower FeO_T/MgO (Fig. 5b). They also have higher contents of TiO_2 (1.56–1.80 wt.%) and incompatible elements than the Gaojiadian and Mataizi dyke samples, and are strongly enriched in LREEs over HREEs, with negligible Eu anomalies (Fig. 6c). In the PM-normalized trace element diagram (Fig. 6d), the Saheqiao samples are relatively enriched in LILEs and depleted in HFSEs, and have positive Sr anomalies. The samples are characterized by a narrow range of initial $^{87}Sr/^{86}Sr$ ratios of 0.703948–0.704604 and negative $\varepsilon_{Nd}(t)$ values of -6.6 to -4.7 with T_{DM} ages of 1537–1381 Ma, when calculated at 223 Ma (Table S7 and Fig. 7).

4 Discussion

4.1 Petrogenesis of Late Triassic mafic dykes in Eastern Hebei

Even though the Late Triassic dykes in Eastern Hebei experienced various degrees of post-magmatic alteration, their major elements and most of their trace elements including LILEs, REEs and HFSEs were essentially immobile during post-magmatic alteration as these samples have relatively low LOI (Table S6) and their trace elements generally correlate positively with Zr (Fig. S1). Therefore, we can trace the magmatic process generating these mafic dykes based on their bulk-rock geochemistry.

4.1.1 Gaojiadian and Mataizi dykes: melting of the enriched lithospheric mantle contaminated by ancient lower crust

The Gaojiadian and Mataizi dykes were coeval (Fig. 3) and have similar bulk-rock geochemical compositions (Figs. 5–7), implying that they were derived from the same mantle source and experienced common post-magmatic processes. Although samples for the Gaojiadian and Mataizi dykes are all mafic in composition, they do not represent primary mantle-derived melts that were in equilibrium with mantle peridotite, because the analyzed samples are characterized by high FeO_T/MgO ratios and relatively low abundances of compatible elements (Hirose and Kushiro, 1993; Table S6 and Fig. 5b, 8a and b). Therefore, shallow level processes, such as fractional crystallization and crustal contamination likely contributed to the compositional evolution of the Gaojiadian and Mataizi dykes.

Three samples of the Gaojiadian dyke have bulk-rock Sr-Nd isotopic compositions similar to those of the sub-continental lithospheric mantle (SCLM) beneath the NCC during the Late Triassic (Fig. 7a), implying their primary derivation from the ancient and enriched SCLM. Samples for the Gaojiadian and Mataizi dykes have similar trace element and Sr-Nd compositions to the Triassic ultramafic-mafic rocks and alkaline complexes in the northern NCC (Figs. 6a, b and 7), which were derived from the ancient lithospheric mantle, metasomatized during previous subduction events. These samples shift from the MORB-OIB array in the Nb/Zr-Th/Zr plot, pointing to a mantle source metasomatized by melts/fluids (Fig. 9a). The $(Hf/Sm)_N$-$(Ta/La)_N$ plot (Fig. 9b) indicates that their mantle source was modified by fluid-related subduction metasomatism rather than melt-related subduction metasomatism or carbonatite metasomatism. Samples for the Gaojiadian and Mataizi dykes show a correlation of Ni and V versus Cr of these samples, implying that they experienced fractional crystallization dominated by clinopyroxene (Fig. 8a and b). Two samples (sample J1503 and J1504) of the Gaojiadian dyke are characterized by more enriched Nd isotopic compositions ($\varepsilon_{Nd}(t)$ = -15.5 to -15.1; Fig. 7a), and thus involvement of other isotopically distinct components (e.g., the ancient lower crust), possibly through contamination, is required to account for the Sr-Nd isotopic characteristics of the Gaojiadian and Mataizi dyke samples. The systematic correlation between $I_{Sr}(t)$ and $\varepsilon_{Nd}(t)$ values and some major elements (e.g., SiO_2 and MgO) observed in these samples also indicates that crustal contamination might have occurred (Figs. 8c and 8d). The Gaojiadian and Mataizi dyke samples plot above the MORB-OIB array and close to the lower crust in the Th/Yb-Nb/Yb plot (Fig. 9c), implying that the lower crust was involved. Contamination by the ancient lower crust could have happened when the primary

SCLM-derived magmas were underplated at the crust-mantle boundary. The Late Triassic primary SCLM-derived magmas in the NCC are characterized by near-chondritic $\varepsilon_{Nd}(t)$ values (Chen et al., 2008), and thus their bulk-rock Nd isotopic compositions were susceptible to contamination by the ancient NCC lower crust with highly negative $\varepsilon_{Nd}(t)$ values in the Late Triassic ($\varepsilon_{Nd}(t)$ = -30; Jahn et al., 1999). Due to the general mafic nature of the lower crust (Rudnick and Gao, 2003), contaminated SCLM-derived magmas would still remain mafic. Contamination by the upper crust might have only played a minor role, as evidenced by the xenocrystic zircons in the Mataizi dyke but no significantly elevated initial $^{87}Sr/^{86}Sr$ ratios in these dykes (Table S7; Figs. 3d and 7a).

Given the fact that the Gaojiadian and Mataizi dykes do not represent primary mantle-derived melts after shallow level processes, it is not feasible to precisely constrain melting conditions. However, these samples have moderate enrichment of LREEs over HREEs and thus accordingly relatively low La/Sm and Sm/Yb ratios (Fig. 9d), pointing to relatively high degree melting of an enriched mantle source with spinel ≥ garnet. Therefore, the parental melt for the Gaojiadian and Mataizi dykes may have been produced at ~70–80 km based on the estimates of the garnet-spinel transition zone in fertile lherzolitic mantle rocks (Duggen et al., 2005; Klemme and O'Neill, 2000). The crystallization conditions of the magmas parental to the Gaojidian dyke can be estimated using the clinopyroxene-liquid thermometer (Putirka, 2008), and the calculation is based on the compositions of clinopyroxene grains with high Mg# (> 70) and the bulk-rock composition (approximating the liquid composition). The calculated crystallization temperature for the Gaojiadian dyke is 1116–1164 °C, corresponding to a mantle source with mantle potential temperatures of 1280–1400 °C (Herzberg et al., 2007), and the crystallization pressure was 2.1–3.8 kbar, corresponding to an upper-crustal depth of 8–14 km (assuming the density of the upper crust = 2.7 g cm^{-3}). The earlier crystallization of plagioclase than clinopyroxene, the lack of hydrous minerals (Fig. 2b) and the relatively low Al_2O_3 contents and slightly negative Eu anomalies in the Gaojiadian dyke samples all indicate that these samples were formed from magmas with low water fugacity (Scaillet and Evans, 1999; Grove et al., 2002). The crystallization conditions of the magmas parental to the Mataizi dyke cannot be well constrained due to the absence of primary magmatic minerals following post-emplacement alteration.

4.1.2 Saheqiao Dyke: melting of the enriched lithospheric mantle

The Saheqiao dyke samples are mafic in composition (Table S6), and have low FeO_T/MgO ratios and relatively high abundances of compatible elements (Figs. 5b, 8a and b), implying that the parental magma of the Saheqiao dyke was a near-primary melt equilibrated with mantle peridotite. Fractional crystallization and crustal contamination made negligible contributions, if any, to the magmatic evolution of the Saheqiao dyke samples, as these are compositionally homogeneous and have no systematic correlation between elements and isotopes (Fig. 8). The Saheqiao dyke samples display enriched bulk-rock Sr-Nd isotopic compositions similar to those of the SCLM (Wu et al., 2006; Yang et al., 2009; Zhang et al., 2008a) and contemporaneous ultramafic-mafic rocks and alkaline complexes where a predominant contribution from the SCLM in the northern NCC has been established (Chen et al., 2008; Niu et al. 2012, 2017; Yang et al., 2012; Zhang et al., 2008a; Zhang, 2009, 2012, 2014; Zhu et al., 2017; Fig. 7). Therefore, it can be concluded that the Saheqiao dyke was derived from the lithospheric mantle.

Re-Os isotopes of peridotite xenoliths entrained in Paleozoic kimberlites in the NCC indicate that the lithospheric mantle underneath the NCC formed in the Archean, but that this Archean lithospheric mantle was partly replaced or metasomatized during the Paleoproterozoic and the Late Triassic continental collisional events as further revealed by Re-Os isotopes of peridotite xenoliths carried in Cenozoic alkali basalts (Gao et al., 2002; Wu et al., 2006, 2019; Zhang et al., 2008a;

Zhu et al., 2020). The Saheqiao dyke samples have Mesoproterozoic bulk-rock Nd depleted mantle model ages (Table S7), implying that their ancient lithospheric mantle source was replaced or metasomatized after its formation in the Archean. These samples also have elevated concentrations of Ba, Th, Sr and LREEs (Fig. 6c and d), which are similar to the Triassic alkaline complexes in the northern NCC. Their trace element systematics reveal that their mantle source was enriched by addition of crust-derived components (most probably subduction-related fluids) (Figs. 9a–9c). The presence of magmatic hornblende in the Saheqiao dyke samples (Fig. 2d) is also indicative of a hydrous mantle source. Additionally, these samples have high Ba/Rb and low Rb/Sr ratios, which are consistent with derivation from an amphibole-bearing mantle source (Fig. 10a). The above lines of reasoning clearly point to a metasomatized or enriched ancient lithospheric mantle source for the Saheqiao dyke.

Compared with the Gaojiadian and Mataizi dyke samples, the Saheqiao dyke samples are characterized by lower Yb concentrations, higher abundances of incompatible elements (Fig. 6) and higher La/Sm and Sm/Yb ratios (Fig. 9d), suggesting that they were produced by lower degree partial melting of an enriched mantle source with garnet > spinel. Therefore, the Saheqiao dyke samples should be also generated at the garnet-spinel transition zone of ~70–80km, but the higher portion of garnet relative to spinel means that their melting pressures were slightly higher than those of the Gaojiadian and Matazi dyke samples. Using PRIMELT3 MEGA software (Herzberg and Asimow, 2015), we obtain primary magma compositions and mantle potential temperatures (T_p = 1362–1443 °C) for the Saheqiao dyke samples. However, due to the hydrous nature of their metasomatized ancient lithospheric mantle source, these temperatures are potentially overestimated and should be corrected by several tens of degrees (Gaetani and Grove, 1998), which will be broadly consistent with the thermal state of the upper mantle (Anderson, 2000). The crystallization conditions of the Saheqiao dyke cannot be well constrained due the post-emplacement greenschist-facies alteration of these samples. However, this dyke is almost coeval with and spatially close to the Gaojiadian dyke and also intruded Neoarchean TTG gneisses, implying that they intruded the upper crust at similar depths.

Overall, the geochemical differences of the studied dykes reflect their different petrogenesis, including mantle source characteristics, melting conditions and crustal contamination. The Gaojiadian and Mataizi dykes (238–234 Ma) originated from the ancient lithospheric mantle under relatively low water fugacity, and experienced contamination by both the ancient lower crust and the upper crust, whereas the Saheqiao dyke (223 Ma) was directly sourced from metasomatized enriched ancient lithospheric mantle under hydrous conditions. These dykes were all produced at depths of ~70–80 km, where the garnet-spinel transition takes place, but the Saheqiao dyke was derived by a lower degree of partial melting at slightly deeper levels than the Gaojiadian and Mataizi dykes. Partial melting of the metasomatized enriched ancient lithospheric mantle was most likely triggered by upwelling of the asthenospheric mantle, as these dyke samples have higher Nb/La ratios than magmas solely derived from the lithospheric mantle, and plot in the lithosphere-asthenosphere interaction field in Fig. 10b. After melt generation, these magmas ascended rapidly and intruded the upper crust. The estimated emplacement depth for these dykes implies that denudation in the northern NCC since the Late Triassic could have been as great as 14 km. This denudation was possibly related to the Yanshanian Orogeny, that affected the NCC throughout the Mesozoic. It is not clear whether the exhumation took place because of extension or compression, which operated at different times between the Triassic and Cretaceous (Yang et al., 2006).

4.2 Modification of the lithosphere beneath the NCC in the Late Triassic

It has been proposed that lithospheric thinning of the NCC was initiated in the Late Triassic (e.g., Wang et al., 2015; Yang and Wu, 2009; Yang et al., 2007). However, it is not clear about the nature of the lithosphere beneath the NCC in the Late Triassic, owing to limited occurrences of Late Triassic magmatism in the NCC (Zhang et al., 2012, 2014) and extensive thinning and replacement of lithosphere beneath the NCC in the Late Mesozoic (Yang and Wu, 2009; Zhang et al., 2014). Therefore, it is still controversial how and to what extent the ancient lithospheric keel beneath the NCC was modified in the Late Triassic.

The thick, cold, rigid and refractory ancient lithospheric mantle beneath the NCC was unlikely to be partially melted to generate magmas unless it experienced decompression, addition of volatiles and/or heating (Fig. 11a; Niu, 2005). Decompression-induced melting is generally accepted as the mechanism for production of abundant mafic magmas at mid-ocean ridges or in rifting environments, but obviously this mechanism alone cannot be applied to the NCC during the Late Triassic. As previously discussed, geochemistry of the Late Triassic mafic dykes in Eastern Hebei indicates that their mantle source was metasomatized by subduction-related fluids, and, in particular, the mantle source of the Saheqiao dyke was also hydrated. The Sr-Nd isotopes and trace element compositions of the Triassic ultramafic-mafic rocks and alkaline complexes in the northern NCC show that their ancient lithospheric mantle source had been modified and enriched by the Triassic (Figs. 7 and 9). Some of these Triassic ultramafic-mafic rocks and alkaline complexes have high Ba/Rb ratios, indicating that their mantle source was hydrated and amphibole-bearing (Fig. 10a). The metasomatic enrichment of ancient lithospheric mantle likely occurred in response to interaction between the NCC and neighboring blocks through subduction and collision in the Late Paleozoic and Triassic (Gao et al., 2002; Wu et al., 2006, 2019). The volatiles (most probably water) released from previously subducted slabs would be carried in hydrous melts/fluids and ascend into the ancient lithospheric mantle, hydrating its lower portions and effectively changing its physical properties (e.g., solidus and viscosity) (Niu, 2005). Consequently, the ancient lithospheric mantle was not as rigid and refractory as before, and thus much easier to be partially melted. This transition may have marked the start of its destabilization, which effectively reduced the thickness of the intact ancient lithospheric mantle (Fig. 11b). The Late Triassic mafic dykes in Eastern Hebei, and most of the Triassic ultramafic-mafic rocks and alkaline complexes in the northern NCC, were generated by melting of the modified and enriched ancient lithospheric mantle with different proportions of garnet and spinel (Fig. 9d), corresponding to the garnet-spinel transition zone at a depth of ~70–80 km (Duggen et al., 2005; Klemme and O'Neill, 2000). Only a few of the Triassic ultramafic-mafic rocks and alkaline complexes in the northern NCC were derived from a garnet lherzolite source (Fig. 9d), which might have resulted from the increased solidus and lower melting capacity of the mantle source at higher pressures. But these garnet lherzolite-sourced rocks still indicate that the ancient lithospheric mantle below the garnet-spinel transition zone was also modified. Thus, it can be deduced that the lower portion of the ancient lithospheric mantle beneath the northern NCC had been metasomatized or modified by addition of volatiles during previous subduction events, and the original intact ancient lithosphere was modified and thinned to ~70–80 km by the Late Triassic, at least in some parts of the northern NCC (e.g., Li et al., 2020).

As well as the addition of volatiles, heating by the upwelling asthenosphere might also have played a role in the modification of the lithosphere beneath the NCC in the Triassic. Some Triassic ultramafic-mafic rocks and alkaline complexes in the northern NCC are characterized by enrichment of Nb relative to La and accordingly high Nb/La ratios (Fig. 10b), implying asthenosphere-lithosphere interaction during their petrogenesis. The compilation of bulk-rock Nd isotopic compositions for Permian–Triassic mantle-derived rocks in the northern NCC shows that $\varepsilon_{Nd}(t)$ values of the Middle–Late Triassic rocks are much more elevated than those of their Permian–Early Triassic counterparts (Fig. 7b). This change is indicative of the emerging contribution of juvenile asthenospheric mantle to the Middle–Late Triassic mantle-derived magmatism in the northern NCC (Fig. 11b). Modification of the lithosphere induced by heating from the upwelling asthenosphere beneath the NCC in the Late Triassic was not limited to the lithospheric mantle, but also involved the ancient lower crust when mantle-derived magmas were underplated at the base of the crust. This involvement has been revealed by recent investigations of Late Triassic ancient lower crust-derived intermediate-felsic rocks in the northern NCC (e.g., Jiang et al., 2007; Li et al., 2020; Ma et al., 2012; Wang et al., 2015; Yang et al., 2007) and lower crustal granulite xenoliths (Shao et al., 2000).

Therefore, compared with the overwhelming lithospheric modification of the NCC in the Late Mesozoic, the modification of the lithosphere beneath the NCC in the Late Triassic was restricted in the northern NCC, but did involve both lithospheric mantle and the crust. The modifying agents of the NCC lithosphere were mainly previously subduction-related melts/fluids and subsequently upwelling juvenile asthenospheric mantle. The ancient lithospheric mantle was metasomatized and hydrated during previous subduction events before the Late Triassic, and the thickness of the intact ancient lithospheric mantle was reduced to ~70–80 km locally in the northern NCC (Fig. 11). The juvenile asthenospheric mantle upwelled and heated the base of the NCC lithosphere, inducing partial melting of the subduction-modified ancient lithospheric mantle and the ancient lower crust, and resulting in the modification of the ancient lithosphere beneath the NCC.

4.3 Implications for lithospheric thinning of the NCC

The NCC was a stable cratonic block after final amalgamation in the Paleoproterozoic (Zhao et al., 2005), but during the Mesozoic its thick (> 180 km), cold and refractory lithospheric mantle was removed and replaced by a thin (< 100 km), hot and fertile lithospheric mantle (Xu, 2001). Subduction and collision of neighboring blocks towards the NCC was the driving force that destabilised the lithosphere beneath the NCC. Before the Late Triassic, these events included the southward subduction of the Paleo-Asian oceanic plate, and subsequent arc-arc and arc-continent collision in the north (Tang et al., 2018; Windley et al., 2007, 2010; Xu et al., 2010, 2013) and the northward subduction of the oceanic plate attached to the Yangtze Craton, and subsequent continental collision with the southern margin of the NCC (Li et al., 1993).

The Late Triassic geodynamics of the NCC were mainly governed by a post-collisional regime after its amalgamation with these neighboring blocks, which was characterized by the shift from compression- to extension-dominated stress fields (Zhang et al., 2014). This transition of stress fields to post-collisional extension is shown by the Late Triassic detachment faults with E-W strikes, metamorphic core complexes, L-tectonites and isolated rift basins in the northern part of the NCC (Davis et al., 2004; Meng et al., 2020; Zhang et al., 2014). There was no mantle plume activity at this time that could have caused extension. During subduction and collision of neighboring blocks towards the NCC in both the south and north in the early Mesozoic, the ancient lithospheric root of the NCC was inevitably modified by subduction-related melts/fluids. Under post-collisional extension in the Late Triassic, there was lithospheric thinning, and passive upwelling of juvenile asthenosphere beneath the NCC. This resulted in the formation of cumulate and granulite xenoliths in the northern NCC (Shao et al., 1999, 2000). The hot ascending asthenosphere heated and induced melting of the subduction-modified ancient lithospheric mantle and the ancient lower crust. Magmas sourced from compositionally distinct reservoirs assimilated in different proportions, generating various kinds of Late Triassic igneous rocks in the NCC. As a result, a Late Triassic EW-trending alkaline/ultramafic-mafic magmatic belt developed along the northern margin of the NCC (Fig. 1a; Chen et al., 2008; Niu et al., 2012, 2017; Yang et al., 2012; Zhang et al., 2008b; Zhang, 2009, 2012, 2014).

5 Conclusions

(1) Late Triassic mafic magmatism in Eastern Hebei is represented by intrusion of mafic dykes during 238–223 Ma with the coeval Gaojiadian and Mataizi dykes intruding Precambrian basement earlier at 238–234 Ma and emplacement of the Saheqiao dyke into Neoarchean supracrustal rocks at 223 ± 4 Ma (2*s*).

(2) These dykes in Eastern Hebei were crystallized from ancient lithospheric mantle-derived magams, and the melting of ancient lithospheric mantle resulted from metasomatism during previous subduction events and heat provided by upwelling asthenosphere. Though these dykes show some compositional variation, their geochemistry indicates that the melting of ancient lithospheric mantle was within the garnet-spinel transition zone (~70–80 km). Constrast in their geochemistry was mainly governed by different melting conditions and post-magmtic processes: the Gaojiadian and Mataizi dykes were generated by relatively higher degrees of partial melting at slightly lower pressures under relatively low water fugacity than the Saheqiao dyke, and further experienced crustal contamination.

(3) The estimated emplacement depth for these dykes is indicative of up to 14 km denudation in the northern NCC since the Late Triassic. The melting conditions of these dykes means that the intact ancient lithospheric mantle had been locally modified or thinned to ~70–80 km by the Late Triassic.

(4) The intrusion of the Late Triassic mafic dykes in Eastern Hebei occurred in a post-collisional

extensional setting, marking the onset of lithospheric thinning of the NCC, which was triggered by subduction and collision of neighboring blocks beneath the NCC.

Acknowledgements

We would like to thank Prof. Simon Wilde and an anonymous reviewer for their thorough and constructive review comments, which significantly improved the quality of this manuscript. Editorial handling by the Editor-in-Chief Prof. Balz Kamber is gratefully acknowledged. This study was financially supported by the National Key Research and Development Program of China (2019YFA0708503), the National Natural Science Foundation of China (grant nos. 41903028, 42030304, 41888101), the Fundamental Research Funds for the Central Universities of China (grant no. 2652018115) and the Presidential Post-doctoral Fellowship of the University of Hong Kong.

References

Aldanmaz, E., Pearce, J.A., Thirlwall, M.F., Mitchell, J.G., 2000. Petrogenetic evolution of late Cenozoic, post-collision volcanism in western Anatolia, Turkey. Journal of Volcanology and Geothermal Research, 102(1): 67-95.

Anderson, D.L., 2000. The thermal state of the upper mantle; No role for mantle plumes. Geophysical Research Letters, 27(22): 3623-3626.

Chen, B., Tian, W., Liu, A.K., 2008. Petrogenesis of the Xiaozhangjiakou Mafic-Ultramafic Complex, North Hebei: Constraints from Petrological, Geochemical and Nd-Sr Isotopic Data. Geological Journal of China Universities, 14 (3): 295-303.

Corfu, F., Hanchar, J.M., Hoskin, P.W., Kinny, P., 2003. Atlas of zircon textures. Reviews in Mineralogy and Geochemistry, 53(1): 469-500.

Davis, G., Xu, B., Zheng, Y.-D., Zhang, W.-J., 2004. Indosinian extension in the Solonkersuture zone: The Sonid Zuoqi metamorphic core complex, Inner Mongolia, China. Dixue Qianyuan(Earth Science Frontiers), 11(3): 135-144.

Duan, Z., Wei, C., Qian, J., 2015. Metamorphic P–T paths and Zircon U–Pb age data for the Paleoproterozoic metabasic dykes of high-pressure granulite facies from Eastern Hebei, North China Craton. Precambrian Research, 271: 295-310.

Duan, Z., Wei, C., Rehman, H.U., 2017. Metamorphic evolution and zircon ages of pelitic granulites in eastern Hebei, North China Craton: Insights into the regional Archean P–T–t history. Precambrian Research, 292: 240-257.

Duggen, S., Hoernle, K., van den Bogaard, P., Garbe-Schönberg, D., 2005. Post-collisional transition from subduction-to intraplate-type magmatism in the westernmost Mediterranean: evidence for continental-edge delamination of subcontinental lithosphere. Journal of Petrology, 46(6): 1155-1201.

Fan, W., Jiang, N., Xu, X., Hu, J., Zong, K., 2017. Petrogenesis of the middle Jurassic appinite and coeval granitoids in the Eastern Hebei area of North China Craton. Lithos, 278–281: 331-346.

Furman, T., Graham, D., 1999. Erosion of lithospheric mantle beneath the East African Rift system: geochemical evidence from the Kivu volcanic province. In: Hilst, R.D.v.d., McDonough, W.F. (Eds.), Developments in Geotectonics. Elsevier, pp. 237-262.

Gaetani, G.A., Grove, T.L., 1998. The influence of water on melting of mantle peridotite. Contributions to Mineralogy and Petrology, 131(4): 323-346.

Gao, S., Rudnick, R.L., Carlson, R.W., McDonough, W.F., Liu, Y.S., 2002. Re–Os evidence for replacement of ancient mantle lithosphere beneath the North China craton. Earth and Planetary Science Letters, 198(3–4): 307-322.

Gao, S. et al., 2004. Recycling lower continental crust in the North China craton. Nature, 432(7019): 892-897.

Grove, T., Parman, S., Bowring, S., Price, R., Baker, M., 2002. The role of an H2O-rich fluid component in the generation of primitive basaltic andesites and andesites from the Mt. Shasta region, N California. Contributions to Mineralogy and Petrology, 142(4): 375-396.

Herzberg, C., Asimow, P.D., 2015. PRIMELT3 MEGA.XLSM software for primary magma calculation: Peridotite primary magma MgO contents from the liquidus to the solidus. Geochemistry, Geophysics, Geosystems, 16(2): 563-578.

Herzberg, C. et al., 2007. Temperatures in ambient mantle and plumes: Constraints from basalts, picrites, and komatiites. Geochemistry, Geophysics, Geosystems, 8(2): Q02006.

Hirose, K., Kushiro, I., 1993. Partial melting of dry peridotites at high pressures: Determination of compositions of melts segregated from peridotite using aggregates of diamond. Earth and Planetary Science Letters, 114(4): 477-489.

Jahn, B.M., Wu, F.Y., Lo, C.H., Tsai, C.H., 1999. Crust–mantle interaction induced by deep subduction of the continental crust: geochemical and Sr–Nd isotopic evidence from post-collisional mafic–ultramafic intrusions of the northern Dabie complex, central China. Chemical Geology, 157(1–2): 119-146.

Jia, L., Wang, L., Wang, G., Lei, S., Wu, X., 2019. Petrogenesis of the Late Triassic shoshonitic Shadegai pluton from the northern North China Craton: Implications for crust-mantle interaction and post-collisional extension. Geoscience Frontiers, 10(2): 595-610.

Jiang, N., Liu, Y.S., Zhou, W.G., Yang, J.H., Zhang, S.Q., 2007. Derivation of Mesozoic adakitic magmas from ancient lower crust in the North China craton. Geochimica et Cosmochimica Acta, 71(10): 2591-2608.

Klemme, S., O'Neill, H.S., 2000. The near-solidus transition from garnet lherzolite to spinel lherzolite. Contributions to Mineralogy and Petrology, 138(3): 237-248.

La Flèche, M.R., Camiré, G., Jenner, G.A., 1998. Geochemistry of post-Acadian, Carboniferous continental intraplate basalts from the Maritimes Basin, Magdalen Islands, Québec, Canada. Chemical Geology, 148(3): 115-136.

Leake, B.E. et al., 2003. Nomenclature of Amphiboles: Additions and Revisions to the International Mineralogical Association's 1997 Recommendations. The Canadian Mineralogist, 41(6): 1355-1362.

Li, R. et al., 2020. Triassic lithospheric modification of the northern North China Craton: Evidences from the composite Kalaqin Batholith and ultramafic-mafic Heilihe Intrusive Complex in Inner Mongolia. Lithos: 105501.

Li, S.-R., Santosh, M., 2017. Geodynamics of heterogeneous gold mineralization in the North China Craton and its relationship to lithospheric destruction. Gondwana Research, 50: 267-292.

Li, S.G. et al., 1993. Collision of the North China and Yangtse Blocks and formation of coesite-bearing eclogites: Timing and processes. Chemical Geology, 109(1–4): 89-111.

Liou, P., Cui, X., Guo, J., Zhai, M., 2020. Possible link between the oldest supracrustal unit and the oldest rock unit of China. Precambrian Research, 342: 105672.

Liou, P., Guo, J., 2019. Generation of Archaean TTG Gneisses Through Amphibole-Dominated Fractionation. Journal of Geophysical Research: Solid Earth, 124(4): 3605-3619.

Liu, D.Y., Nutman, A.P., Compston, W., Wu, J.S., Shen, Q.H., 1992. Remnants of ≥3800 Ma crust in the Chinese part of the Sino-Korean craton. Geology, 20(4): 339-342.

Liu, J., Cai, R., Pearson, D.G., Scott, J.M., 2019. Thinning and destruction of the lithospheric mantle root beneath the North China Craton: A review. Earth-Science Reviews, 196: 102873.

Liu, J., Davis, G.A., Ji, M., Guan, H., Bai, X., 2008. Crustal Detachment and Destruction of the Keel of North China Craton: Constraints from Late Mesozoic Extensional Structures. Earth Science Frontiers, 15(3): 72-81.

Liu, J. et al., 2020. Destruction of the Northern Margin of the North China Craton in Mid-Late Triassic: Evidence from Asthenosphere-Derived Mafic Enclaves in the Jiefangyingzi Granitic Pluton from Chifeng Area, Southern Inner Mongolia. Acta Geologica Sinica - English Edition, n/a(n/a).

Liu, S. et al., 2018. Integrated elemental and Sr-Nd-Pb-Hf isotopic studies of Mesozoic mafic dykes from the eastern North China Craton: implications for the dramatic transformation of lithospheric mantle. Journal of Geodynamics, 114: 19-40.

Ma, L. et al., 2014a. Lithospheric and asthenospheric sources of lamprophyres in the Jiaodong Peninsula: A consequence of rapid lithospheric thinning beneath the North China Craton? Geochimica et Cosmochimica Acta, 124: 250-271.

Ma, L. et al., 2016. Rapid lithospheric thinning of the North China Craton: New evidence from cretaceous mafic dikes in the Jiaodong Peninsula. Chemical Geology, 432: 1-15.

Ma, L. et al., 2014b. Geochemistry of Early Cretaceous calc-alkaline lamprophyres in the Jiaodong Peninsula: Implication for lithospheric evolution of the eastern North China Craton. Gondwana Research, 25(2): 859-872.

Ma, Q. et al., 2012. Triassic “adakitic” rocks in an extensional setting (North China): Melts from the cratonic lower crust. Lithos, 149(0): 159-173.

Meng, Q.-R., Wu, G.-L., Fan, L.-G., Wei, H.-H., Wang, E., 2020. Late Triassic uplift, magmatism and extension of the northern North China block: Mantle signatures in the surface. Earth and Planetary Science Letters, 547: 116451.

Miyashiro, A., 1974. Volcanic rock series in island arcs and active continental margins. American Journal of Science, 274(4): 321-355.

Morimoto, N., 1989. Nomenclature of pyroxenes. Mineralogical Journal, 14(5): 198-221.

Niu, X., Chen, B., Feng, G., Liu, F., Yang, J., 2017. Origin of lamprophyres from the northern margin of the North China Craton: implications for mantle metasomatism. Journal of the Geological Society, 174(2): 353-364.

Niu, X., Chen, B., Liu, A., Suzuki, K., Ma, X., 2012. Petrological and Sr–Nd–Os isotopic constraints on the origin of the Fanshan ultrapotassic complex from the North China Craton. Lithos, 149(0): 146-158.

Niu, Y., 2005. Generation and evolution of basaltic magmas: some basic concepts and a new view on the origin of Mesozoic–Cenozoic basaltic volcanism in eastern China. Geological Journal of China Universities, 11(1): 9-46.

Niu, Y., 2014. Geological understanding of plate tectonics: basic concepts, illustrations, examples and new perspectives. Global tectonics and metallogeny., 10(1): 23-46.

Nutman, A.P. et al., 2011. Multistage late Neoarchaean crustal evolution of the North China Craton, eastern Hebei. Precambrian Research, 189(1–2): 43-65.

Pearce, J.A., 2008. Geochemical fingerprinting of oceanic basalts with applications to ophiolite classification and the search for Archean oceanic crust. Lithos, 100(1): 14-48.

Peng, P. et al., 2012. Genesis of the Hengling magmatic belt in the North China Craton: Implications for Paleoproterozoic tectonics. Lithos, 148(0): 27-44.

Putirka, K.D., 2008. Thermometers and barometers for volcanic systems. Reviews in Mineralogy and Geochemistry, 69(1): 61-120.

Rudnick, R.L., Gao, S., 2003. Composition of the continental crust, Treatise on Geochemistry, pp.

1-64.

Santosh, M., Wilde, S.A., Li, J.H., 2007. Timing of Paleoproterozoic ultrahigh-temperature metamorphism in the North China Craton: Evidence from SHRIMP U–Pb zircon geochronology. Precambrian Research, 159(3–4): 178-196.

Scaillet, B., Evans, B.W., 1999. The 15 June 1991 Eruption of Mount Pinatubo. I. Phase Equilibria and Pre-eruption P–T–fO2–fH2O Conditions of the Dacite Magma. Journal of Petrology, 40(3): 381-411.

Shao, J.A., Han, Q.J., Li, H.M., 2000. Discovery of the Early Mesozoic granulite xenoliths in North China Craton. Science in China Series D: Earth Sciences, 43(1): 245-252.

Shao, J.A., Han, Q.J., Zhang, L.Q., Mu, B.L., 1999. Cumulate complex xenoliths in the Early Mesozoic in eastern Inner Mongolia. Chinese Science Bulletin, 44(14): 1272-1279.

Smith, E.I., Sanchez, A., Walker, J.D., Wang, K., 1999. Geochemistry of mafic magmas in the Hurricane Volcanic field, Utah: implications for small-and large-scale chemical variability of the lithospheric mantle. The Journal of geology, 107(4): 433-448.

Smith, J.V., Brown, W.L., 1988. Feldspar Minerals: 1. Crystal Structures, Physical, Chemical, and Microtextural Properties. Heidelberg and New York (Springer-Verlag), Berlin.

Sun, S.S., McDonough, W.F., 1989. Chemical and isotopic systematics of oceanic basalts: implications for mantle composition and processes. Geological Society, London, Special Publications, 42(1): 313-345.

Tam, P.Y. et al., 2011. Timing of metamorphism in the Paleoproterozoic Jiao-Liao-Ji Belt: New SHRIMP U–Pb zircon dating of granulites, gneisses and marbles of the Jiaobei massif in the North China Craton. Gondwana Research, 19(1): 150-162.

Tang, J., Xu, W., Wang, F., Ge, W., 2018. Subduction history of the Paleo-Pacific slab beneath

Eurasian continent: Mesozoic-Paleogene magmatic records in Northeast Asia. Science China Earth Sciences, 61(5): 527-559.

Wan, L. et al., 2019. Geochemistry of middle-late Mesozoic mafic intrusions in the eastern North China Craton: New insights on lithospheric thinning and decratonization. Gondwana Research, 73: 153-174.

Wan, Y.S. et al., 2011. ~2.7 Ga juvenile crust formation in the North China Craton (Taishan-Xintai area, western Shandong Province): Further evidence of an understated event from U–Pb dating and Hf isotopic composition of zircon. Precambrian Research, 186(1–4): 169-180.

Wang, C. et al., 2017. Long-lived melting of ancient lower crust of the North China Craton in response to paleo-Pacific plate subduction, recorded by adakitic rhyolite. Lithos, 292(Supplement C): 437-451.

Wang, C., Song, S., Niu, Y., Su, L., 2015. Late Triassic adakitic plutons within the Archean terrane of the North China Craton: Melting of the ancient lower crust at the onset of the lithospheric destruction. Lithos, 212-215: 353-367.

Wang, C., Song, S., Niu, Y., Wei, C., Su, L., 2016. TTG and Potassic Granitoids in the Eastern North China Craton: Making Neoarchean Upper Continental Crust during Micro-continental Collision and Post-collisional Extension. Journal of Petrology, 57(9): 1775-1810.

Wang, C. et al., 2019. Palaeoarchaean deep mantle heterogeneity recorded by enriched plume remnants. Nature Geoscience, 12(8): 672-678.

Wang, X. et al., 2020. Initiation of the North China Craton destruction: Constraints from the diamond-bearing alkaline basalts from Lan'gan, China. Gondwana Research, 80: 228-243.

Wang, Y., Zhou, L., Liu, S., Li, J., Yang, T., 2018. Post-cratonization deformation processes and tectonic evolution of the North China Craton. Earth-Science Reviews, 177: 320-365.

Winchester, J.A., Floyd, P.A., 1977. Geochemical discrimination of different magma series and their differentiation products using immobile elements. Chemical Geology, 20: 325-343.

Windley, B.F., Alexeiev, D., Xiao, W., Kröner, A., Badarch, G., 2007. Tectonic models for accretion of the Central Asian Orogenic Belt. Journal of the Geological Society, 164(1): 31-47.

Windley, B.F., Maruyama, S., Xiao, W.J., 2010. Delamination/thinning of sub-continental lithospheric mantle under Eastern China: The role of water and multiple subduction. American Journal of Science, 310(10): 1250-1293.

Wu, F.-Y., Walker, R.J., Yang, Y.-H., Yuan, H.-L., Yang, J.-H., 2006. The chemical-temporal evolution of lithospheric mantle underlying the North China Craton. Geochimica et Cosmochimica Acta, 70(19): 5013-5034.

Wu, F.-Y., Yang, J.-H., Xu, Y.-G., Wilde, S.A., Walker, R.J., 2019. Destruction of the North China Craton in the Mesozoic. Annual Review of Earth and Planetary Sciences, 47(1): 173-195.

Wu, F.Y., Lin, J.Q., Wilde, S.A., Zhang, X.O., Yang, J.H., 2005. Nature and significance of the Early Cretaceous giant igneous event in eastern China. Earth and Planetary Science Letters, 233(1–2): 103-119.

Xiong, L. et al., 2018. Geochronology, petrology and geochemistry of the Mesozoic Dashizhuzi granites and lamprophyre dykes in eastern Hebei–western Liaoning: implications for lithospheric evolution beneath the North China Craton. Geological Magazine, 155(7): 1542-1565.

Xu, W.-L. et al., 2013. Spatial–temporal relationships of Mesozoic volcanic rocks in NE China: Constraints on tectonic overprinting and transformations between multiple tectonic regimes. Journal of Asian Earth Sciences, 74: 167-193.

Xu, W., Yang, D., Gao, S., Pei, F., Yu, Y., 2010. Geochemistry of peridotite xenoliths in Early Cretaceous high-Mg# diorites from the Central Orogenic Block of the North China Craton: the nature of Mesozoic lithospheric mantle and constraints on lithospheric thinning. Chemical Geology, 270(1-4): 257-273.

Xu, Y., Li, H., Pang, C., He, B., 2009. On the timing and duration of the destruction of the North China Craton. Chinese Science Bulletin, 54(19): 3379-3396.

Xu, Y.G., 2001. Thermo-tectonic destruction of the archaean lithospheric keel beneath the sino-korean craton in china: evidence, timing and mechanism. Physics and Chemistry of the Earth, Part A: Solid Earth and Geodesy, 26(9–10): 747-757.

Xue, F., Santosh, M., Tsunogae, T., Yang, F., 2019. Geochemical and isotopic imprints of early Cretaceous mafic and felsic dyke suites track lithosphere-asthenosphere interaction and craton destruction in the North China Craton. Lithos, 326-327: 174-199.

Yang, C.-X., Santosh, M., 2020. Ancient deep roots for Mesozoic world-class gold deposits in the north China craton: An integrated genetic perspective. Geoscience Frontiers, 11(1): 203-214.

Yang, C., Wei, C., 2017a. Two phases of granulite facies metamorphism during Neoarchean and Paleoproterozoic in the East Hebei, North China Craton: records from mafic granulites. Precambrian Research, 301: 49-64.

Yang, C., Wei, C., 2017b. Ultrahigh temperature (UHT) mafic granulites in the East Hebei, North China Craton: Constraints from a comparison between temperatures derived from REE-based thermometers and major element-based thermometers. Gondwana Research, 46: 156-169.

Yang, J.-H., Sun, J.-F., Zhang, M., Wu, F.-Y., Wilde, S.A., 2012. Petrogenesis of silica-saturated and silica-undersaturated syenites in the northern North China Craton related to post-collisional and intraplate extension. Chemical Geology, 328: 149-167.

Yang, J., Wu, F., Zhang, Y., Zhang, Q., Wilde, S.A., 2004. Identification of Mesoproterozoic zircons in a Triassic dolerite from the Liaodong Peninsula, Northeast China. Chinese Science Bulletin, 49(18): 1958-1962.

Yang, J.H. et al., 2010. Diachronous decratonization of the Sino-Korean craton: Geochemistry of mantle xenoliths from North Korea. Geology, 38(9): 799-802.

Yang, J.H. et al., 2006. Constraints on the timing of uplift of the Yanshan Fold and Thrust Belt, North China. Earth and Planetary Science Letters, 246(3–4): 336-352.

Yang, J.H., Wu, F.Y., 2009. Triassic magmatism and its relation to decratonization in the eastern North China Craton. Science in China Series D: Earth Sciences, 52(9): 1319-1330.

Yang, J.H., Wu, F.Y., Wilde, S.A., 2003. A review of the geodynamic setting of large-scale Late Mesozoic gold mineralization in the North China Craton: an association with lithospheric thinning. Ore Geology Reviews, 23(3–4): 125-152.

Yang, J.H., Wu, F.Y., Wilde, S.A., Belousova, E., Griffin, W.L., 2008. Mesozoic decratonization of the North China block. Geology, 36(6): 467-470.

Yang, J.H., Wu, F.Y., Wilde, S.A., Liu, X.M., 2007. Petrogenesis of Late Triassic granitoids and their enclaves with implications for post-collisional lithospheric thinning of the Liaodong Peninsula, North China Craton. Chemical Geology, 242(1–2): 155-175.

Yang, Y.-H. et al., 2009. In situ perovskite Sr–Nd isotopic constraints on the petrogenesis of the Ordovician Mengyin kimberlites in the North China Craton. Chemical Geology, 264(1–4): 24-42.

Zhang, H.-F. et al., 2008a. Evolution of subcontinental lithospheric mantle beneath eastern China: Re–Os isotopic evidence from mantle xenoliths in Paleozoic kimberlites and Mesozoic basalts. Contributions to Mineralogy and Petrology, 155(3): 271-293.

Zhang, H.F., Zhou, M.F., Sun, M., Zhou, X.H., 2010. The origin of Mengyin and Fuxian diamondiferous kimberlites from the North China Craton: Implication for Palaeozoic subducted oceanic slab–mantle interaction. Journal of Asian Earth Sciences, 37(5–6): 425-437.

Zhang, K.-J., 2012. Destruction of the North China Craton: Lithosphere folding-induced removal of lithospheric mantle? Journal of Geodynamics, 53: 8-17.

Zhang, S.-H., Zhao, Y., Davis, G.A., Ye, H., Wu, F., 2014. Temporal and spatial variations of Mesozoic magmatism and deformation in the North China Craton: Implications for lithospheric thinning and decratonization. Earth-Science Reviews, 131(0): 49-87.

Zhang, S.-H., Zhao, Y., Li, X.-H., Ernst, R.E., Yang, Z.-Y., 2017. The 1.33–1.30 Ga Yanliao large igneous province in the North China Craton: Implications for reconstruction of the Nuna (Columbia) supercontinent, and specifically with the North Australian Craton. Earth and Planetary Science Letters, 465(Supplement C): 112-125.

Zhang, S.-H. et al., 2009. Contrasting Late Carboniferous and Late Permian–Middle Triassic intrusive suites from the northern margin of the North China craton: Geochronology, petrogenesis, and tectonic implications. Geological Society of America Bulletin, 121(1-2): 181-200.

Zhang, S.-H., Zhao, Y., Ye, H., Hou, K.-J., Li, C.-F., 2012. Early Mesozoic alkaline complexes in the northern North China Craton: Implications for cratonic lithospheric destruction. Lithos, 155(0): 1-18.

Zhang, X.H., Zhang, H., Zhai, M., Wilde, S.A., Xie, L., 2008b. Geochemistry of Middle Triassic gabbros from northern Liaoning, North China: origin and tectonic implications. Geological Magazine, 146(4): 540-551.

Zhao, G.C., Sun, M., Wilde, S.A., Li, S.Z., 2005. Late Archean to Paleoproterozoic evolution of the North China Craton: key issues revisited. Precambrian Research, 136(2): 177-202.

Zhao, J.-H., Zhou, M.-F., 2007. Geochemistry of Neoproterozoic mafic intrusions in the Panzhihua district (Sichuan Province, SW China): Implications for subduction-related metasomatism in the upper mantle. Precambrian Research, 152(1): 27-47.

Zhu, R., Xu, Y., 2019. The subduction of the west Pacific plate and the destruction of the North China Craton. Science China Earth Sciences, 62(9): 1340-1350.

Zhu, Y.-S., Yang, J.-H., Sun, J.-F., Wang, H., 2017. Zircon Hf-O isotope evidence for recycled oceanic and continental crust in the sources of alkaline rocks. Geology, 45(5): 407-410.

Zhu, Y.-S., Yang, J.-H., Wang, H., Wu, F.-Y., 2020. Mesoproterozoic (~ 1.32 Ga) modification of lithospheric mantle beneath the North China Craton caused by break-up of the Columbia supercontinent. Precambrian Research: 105674.

Figure captions

Fig. 1. (a) Simplified tectonic map of north Asia. (b) Schematic geological map of Eastern Hebei, the NCC; (c) and (d) Geological maps of the study area in Eastern Hebei, the NCC.

Fig. 2. (a), (c) and (e) Field photos of the Gaojiadian dyke, the Saheqiao dyke and the Mataizi dyke, respectively, which intruded the Neoarchaean TTG/supracrustal gneisses. (b), (d) and (f) Photomicrographs showing the petrographic features of the Gaojiadian dyke (cross-polarized light), the Saheqiao dyke (plane-polarized light) and the Mataizi dyke (plane-polarized light), respectively. Note the presence of igneous zircons in the Gaojiadian and the Saheqiao dyke samples. Cpx, clinopyroxene; Hb, hornblende; Pl, plagioclase; Ab, albite; Act, actinolite; Zrn, zircon.

Fig. 3. (a) Cathodoluminescence images of representative zircons from the Gaojiadian dyke sample J1416, the Saheqiao dyke sample 15SHQ05 and the Mataizi dyke sample 18NC51. The ellipses (about 20×30 μm in size; SIMS) and circles (about 36 μm in diameter; LA-ICPMS) are *in situ* zircon U–Pb analytical spots with numbers of analytical spots (Tables S1–S2). The ages below the cathodoluminescence images are $^{206}Pb/^{238}U$ ages for magmatic zircons and $^{207}Pb/^{206}Pb$ ages for xenocrystic zircons (Tables S1 and S2). Scale bars, 100 μm. (b)–(d) U-Pb concordia diagrams for zircons from the Gaojiadian dyke sample J1416, the Saheqiao dyke sample 15SHQ05 and the Mataizi dyke sample 18NC51, respectively. Data-point error ellipses in (b)–(d) are at 2*s*. Insets in (b) and (c) are the $^{206}Pb/^{238}U$ ages of individual analyses at 2*s* with weighted mean $^{206}Pb/^{238}U$ ages of zircons at 95% confidence level.

Fig. 4. (a) Wo-En-Fs diagram (Morimoto, 1989) for clinopyroxene from the Gaojiadian dyke sample J1416. (b) An-Ab-Or diagram (Smith and Brown, 1988) for plagioclase from the Gaojiadian dyke sample J1416. (c) X_{Mg}-Si diagram (Leake et al., 2003) for magmatic hornblende from the Saheqiao dyke sample 15SHQ03.

Fig. 5. (a) Rock classification diagram (Winchester and Floyd, 1977), and (b) FeO_T/MgO-SiO_2 diagram (Miyashiro, 1974) for the Late Triassic mafic dykes in Eastern Hebei.

Fig. 6. (a) Chondrite-normalized REE patterns, and (b) primitive mantle-normalized trace element diagram for the Late Triassic Gaojiadian and Mataizi dykes in Eastern Hebei. (c) Chondrite-normalized REE patterns, and (d) primitive mantle-normalized trace element diagram for the Late

Triassic Saheqiao dyke in Eastern Hebei. The values of chondrite and primitive mantle are from Sun and McDonough (1989). Trace element compositions of Triassic ultramafic-mafic rocks and alkaline complexes in the northern NCC are also plotted for comparison. Data sources: Chen et al. (2008); Li et al. (2020); Liu et al. (2020); Niu et al. (2012, 2017); Yang et al. (2012); Zhang et al. (2008b); Zhang (2009, 2012, 2014); Zhu et al. (2017) and references therein.

Fig. 7. (a) $\varepsilon_{Nd}(t)$-$I_{Sr}(t)$ diagram for the Late Triassic mafic dykes in Eastern Hebei. Also plotted for comparison are the Sr-Nd isotopic compositions of different reservoirs, including the sub-continental lithospheric mantle (SCLM) beneath the NCC (approximated by peridotite xenoliths and perovskites in Paleozoic kimberlites; Wu et al., 2006; Yang et al., 2009; Zhang et al., 2008a and references therein), the lower continental crust (LCC) and the upper continental crust (UCC) of the NCC (Jahn et al., 1999). Fields of MORB and OIB are constructed using the data from the PetDB database (https://www.earthchem.org/petdb). All data are calculated at 234 Ma. (b) ε_{Nd}-t diagram for the Late Triassic mafic dykes in Eastern Hebei. Sr-Nd isotopic compositions of Permian–Triassic ultramafic-mafic rocks and alkaline complexes in the northern NCC are also plotted for comparison. Data sources are the same as in Fig. 6.

Fig. 8. Co-variation diagrams of (a) Ni-Cr, (b) V-Cr, (c) $I_{Sr}(t)$-SiO_2 and (d) $\varepsilon_{Nd}(t)$-MgO for the Late Triassic mafic dykes in Eastern Hebei. The clinopyroxene-dominated fractionation for the Gaojiadian dyke samples is shown in (a) and (b). The correlation between $I_{Sr}(t)$ and $\varepsilon_{Nd}(t)$ values and major element oxides for the Gaojiadian dyke and the Mataizi dyke samples in (c) and (d) implies crustal contamination. Note that sample 15SHQ04 and 15SHQ05 have similar MgO contents and $\varepsilon_{Nd}(t)$ values, which overlap in (d).

Fig. 9. Co-variation diagrams of (a) Nb/Zr-Th/Zr (Zhao and Zhou, 2007), (b) $(Hf/Sm)_N$-$(Ta/La)_N$ (La Flèche et al., 1998), (c) Th/Yb-Nb/Yb (Pearce, 2008) and (d) Sm/Yb-La/Sm (Aldanmaz et al., 2000) for the Late Triassic mafic dykes in Eastern Hebei. Trace element compositions of Triassic ultramafic-mafic rocks and alkaline complexes in the northern NCC are also plotted for comparison. Data sources are the same in as Fig. 6. In (d), melting curves of lherzolite containing garnet, spinel or garnet + spinel are after Aldanmaz et al. (2000); numbers along melting curves are degrees of partial melting. The values of PM, N-MORB, E-MORB and OIB are from Sun and McDonough (1989) and the values of continental crust (CC), lower continental crust (LCC) and upper continental crust (UCC) are from Rudnick and Gao (2003).

Fig. 10. Co-variation diagrams of (a) Rb/Sr-Ba/Rb (Furman and Graham, 1999) and (b) Nb/La-La/Yb (Smith et al., 1999) for the Late Triassic mafic dykes in Eastern Hebei. The trends in (a) indicate the possible hydrous phases present in the mantle source of the magmas. Note that in (a) sample 18NC66 is omitted because of its high Ba/Rb ratios. Trace element compositions of Triassic ultramafic-mafic rocks and alkaline complexes in the northern NCC are also plotted for comparison. Data sources are the same in as Fig. 6.

Fig. 11. Illustration of the petrogenesis of the Late Triassic mafic dykes in Eastern Hebei, NCC. (a) In the Paleozoic, the NCC had a thick, cold and refractory ancient sub-continental lithospheric mantle (SCLM). (b) The lower portion of the ancient SCLM was metasomatized by volatiles (most probably water; yellow dots) released from subducted slabs before the Late Triassic, and this

modified ancient SCLM was no longer as rigid and refractory as before because its solidus and viscosity were lowered by the addition of volatiles. As a result, the thickness of the intact ancient SCLM had been locally reduced to ~70–80 km. The convective asthenosphere upwelled, and heated the modified SCLM. This then experienced partial melting within the garnet-spinel transition zone (~70–80 km), generating the Saheqiao (at slightly higher pressures and deeper) and the Gaojiadian/Mataizi dykes. (c) The parental magma of the Saheqiao dyke ascended rapidly into the upper crust (Neoarchean TTG gneisses), while the parental magma of the Gaojiadian/Mataizi dyke pondered at the crust/mantle interface and experienced contamination by the mafic ancient lower crust, and then also intruded the Neoarchean TTG/supracrustal gneisses at the upper crustal level.

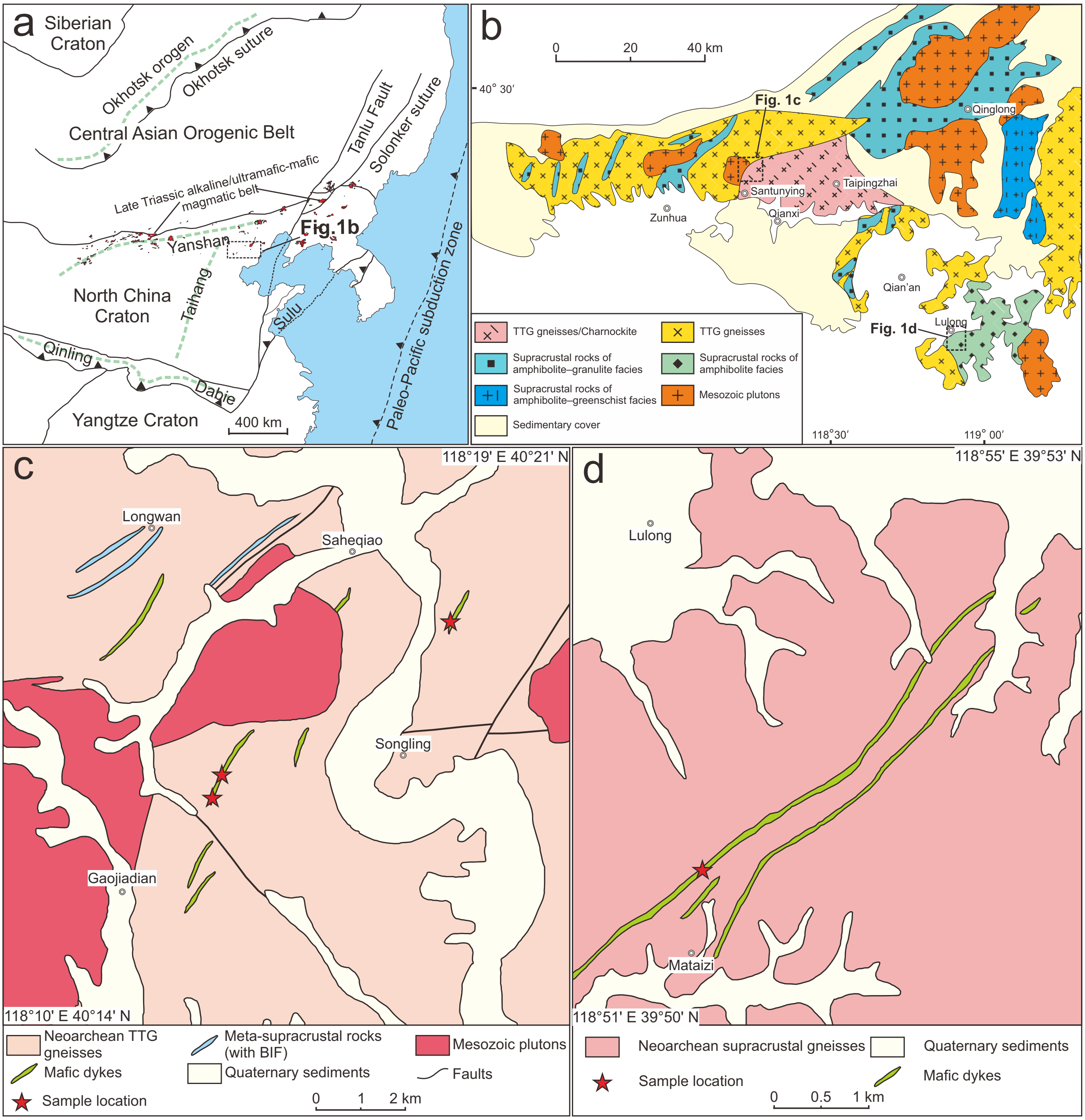
a
Siberian Craton
Okhotsk orogen
Okhotsk suture
Central Asian Orogenic Belt
Tanlu Fault
Solonker suture
Late Triassic alkaline/ultramafic-mafic magmatic belt
Yanshan
Fig.1b
North China Craton
Taihang
Sulu
Paleo-Pacific subduction zone
Qinling
Dabie
Yangtze Craton
400 km
b
0 20 40 km
40° 30′
Fig. 1c
Qinglong
Santunying
Taipingzhai
Zunhua
Qianxi
Qian'an
Fig. 1d
Lulong
TTG gneisses/Charnockite
TTG gneisses
Supracrustal rocks of amphibolite–granulite facies
Supracrustal rocks of amphibolite facies
Supracrustal rocks of amphibolite–greenschist facies
Mesozoic plutons
Sedimentary cover
118°30′
119° 00′
c
118°19' E 40°21' N
Longwan
Saheqiao
Songling
Gaojiadian
118°10' E 40°14' N
Neoarchean TTG gneisses
Meta-supracrustal rocks (with BIF)
Mesozoic plutons
Mafic dykes
Quaternary sediments
Faults
Sample location
0 1 2 km
d
118°55' E 39°53' N
Lulong
Mataizi
118°51' E 39°50' N
Neoarchean supracrustal gneisses
Quaternary sediments
Sample location
Mafic dykes
0 0.5 1 km

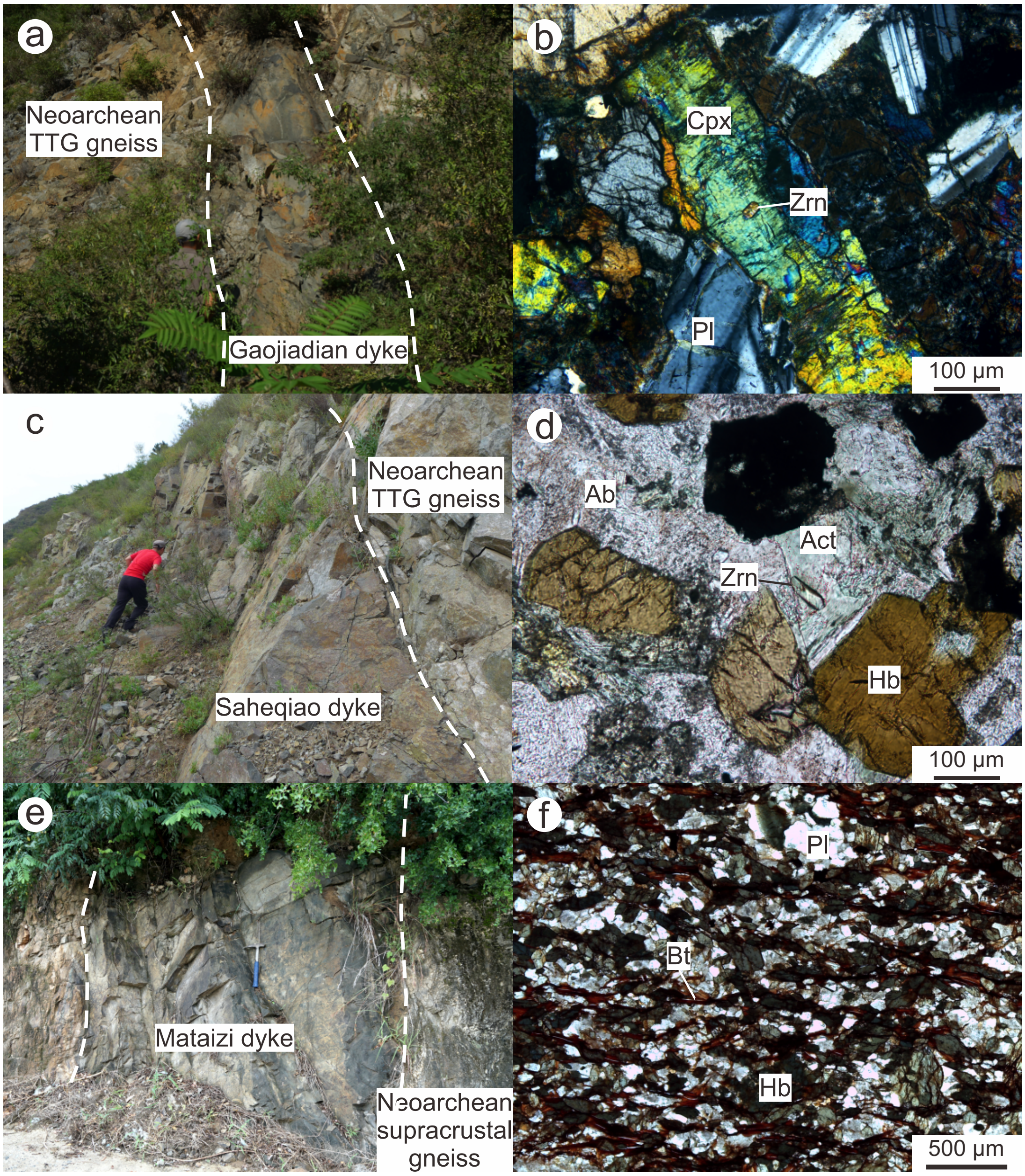
a
Neoarchean
TTG gneiss
Gaojiadian dyke
b
Cpx
Zrn
Pl
100 μm
c
Neoarchean
TTG gneiss
Saheqiao dyke
d
Ab
Act
Zrn
Hb
100 μm
e
Mataizi dyke
Neoarchean
supracrustal
gneiss
f
Pl
Bt
Hb
500 μm

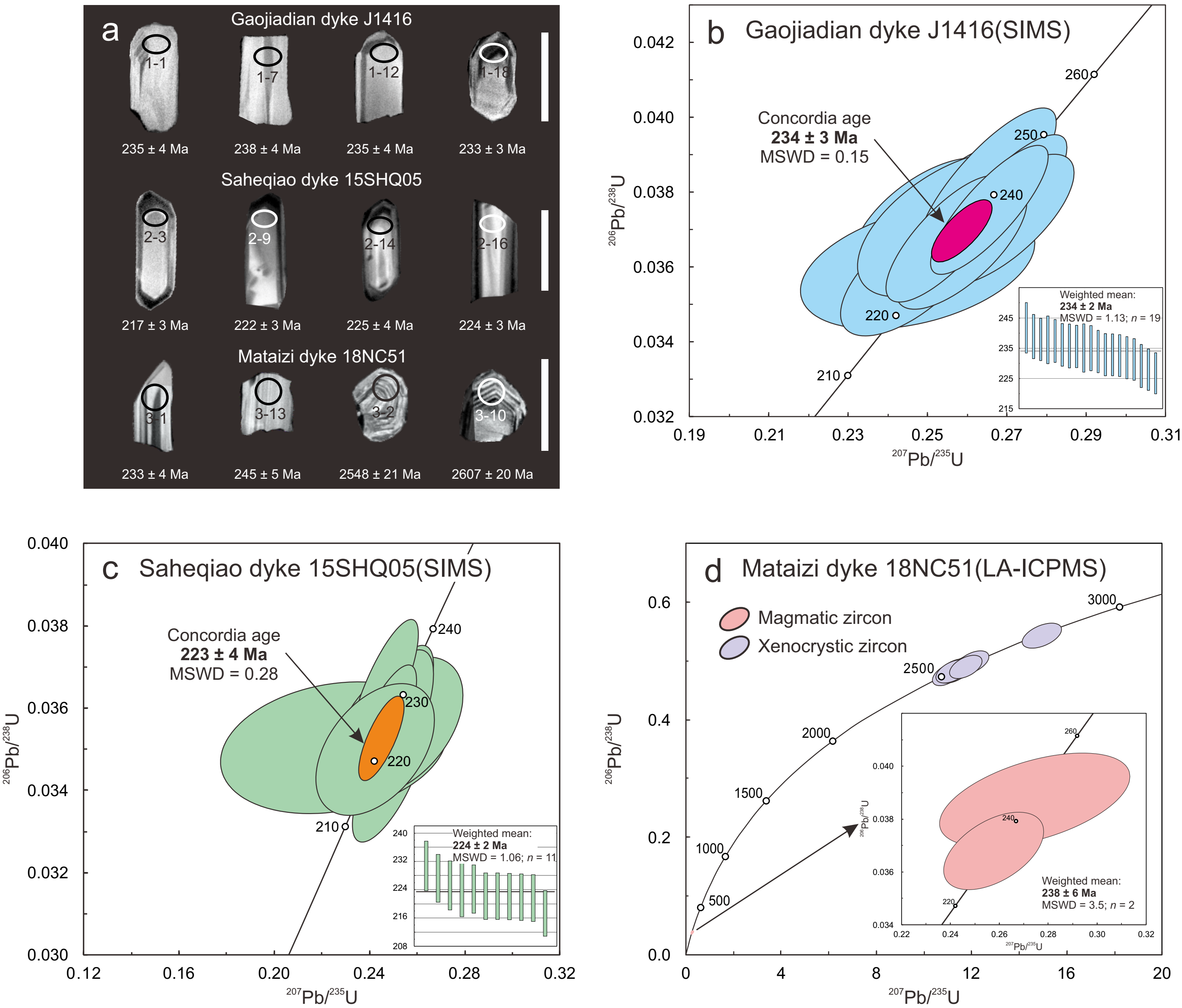

a
Gaojiadian dyke J1416
1-1
1-7
1-12
1-18
235 ± 4 Ma
238 ± 4 Ma
235 ± 4 Ma
233 ± 3 Ma
Saheqiao dyke 15SHQ05
2-3
2-9
2-14
2-16
217 ± 3 Ma
222 ± 3 Ma
225 ± 4 Ma
224 ± 3 Ma
Mataizi dyke 18NC51
3-1
3-13
3-2
3-10
233 ± 4 Ma
245 ± 5 Ma
2548 ± 21 Ma
2607 ± 20 Ma
b
Gaojiadian dyke J1416(SIMS)
Concordia age
234 ± 3 Ma
MSWD = 0.15
Weighted mean:
234 ± 2 Ma
MSWD = 1.13; n = 19
206Pb/238U
207Pb/235U
c
Saheqiao dyke 15SHQ05(SIMS)
Concordia age
223 ± 4 Ma
MSWD = 0.28
Weighted mean:
224 ± 2 Ma
MSWD = 1.06; n = 11
206Pb/238U
207Pb/235U
d
Mataizi dyke 18NC51(LA-ICPMS)
Magmatic zircon
Xenocrystic zircon
Weighted mean:
238 ± 6 Ma
MSWD = 3.5; n = 2
206Pb/238U
207Pb/235U

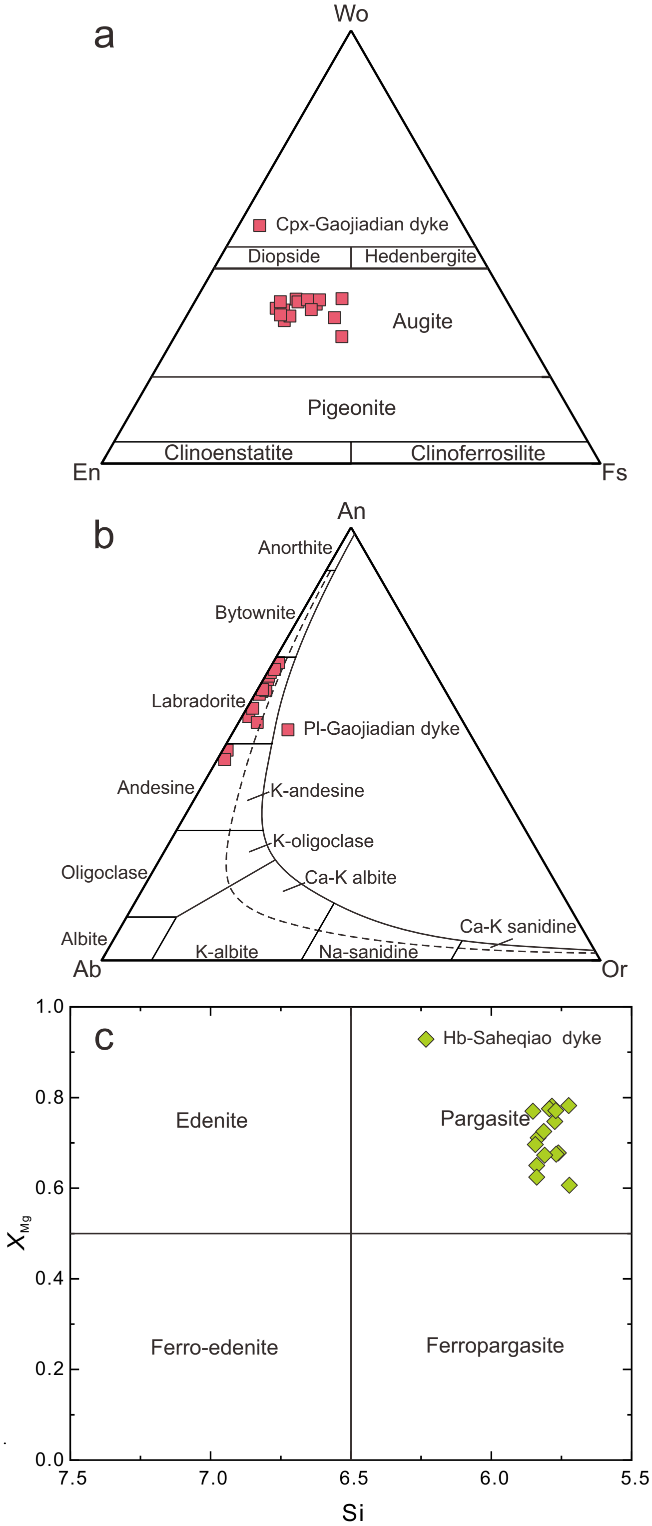
a
Wo
Cpx-Gaojiadian dyke
Diopside
Hedenbergite
Augite
Pigeonite
Clinoenstatite
Clinoferrosilite
En
Fs
b
An
Anorthite
Bytownite
Labradorite
Pl-Gaojiadian dyke
Andesine
K-andesine
K-oligoclase
Oligoclase
Ca-K albite
Ca-K sanidine
Albite
K-albite
Na-sanidine
Ab
Or
c
Hb-Saheqiao dyke
Edenite
Pargasite
Ferro-edenite
Ferropargasite
X Mg
Si
1.0
0.8
0.6
0.4
0.2
0.0
7.5
7.0
6.5
6.0
5.5

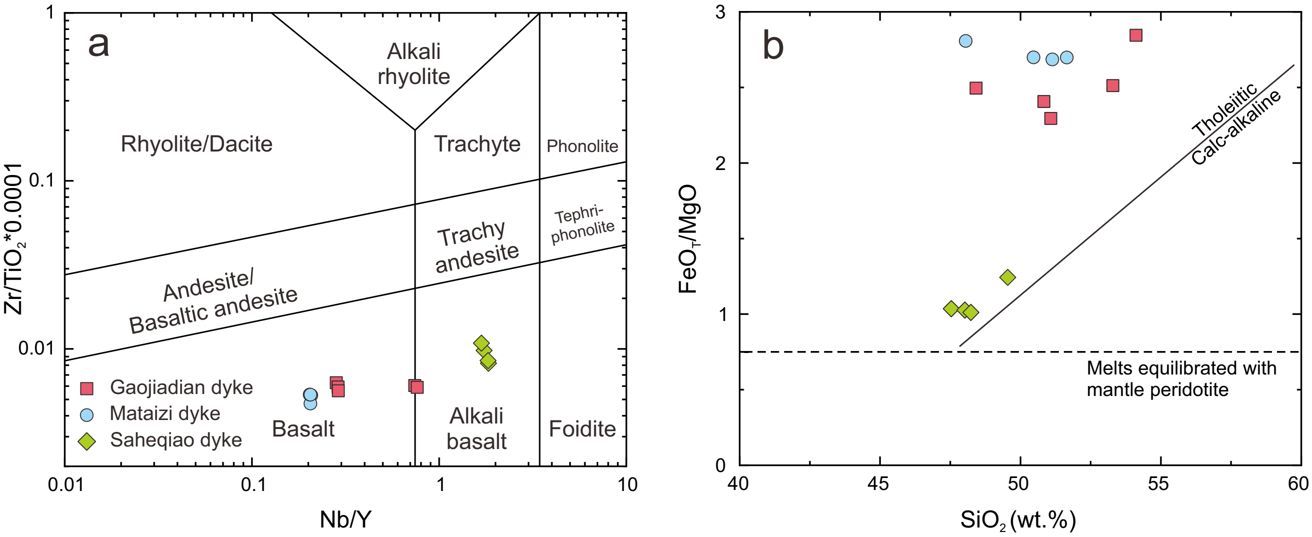

a
Alkali rhyolite
Rhyolite/Dacite
Trachyte
Phonolite
Tephri-phonolite
Trachy andesite
Andesite/ Basaltic andesite
Gaojiadian dyke
Mataizi dyke
Saheqiao dyke
Basalt
Alkali basalt
Foidite
Zr/TiO2*0.0001
Nb/Y
b
Tholeiitic
Calc-alkaline
Melts equilibrated with mantle peridotite
FeOT/MgO
SiO2 (wt.%)

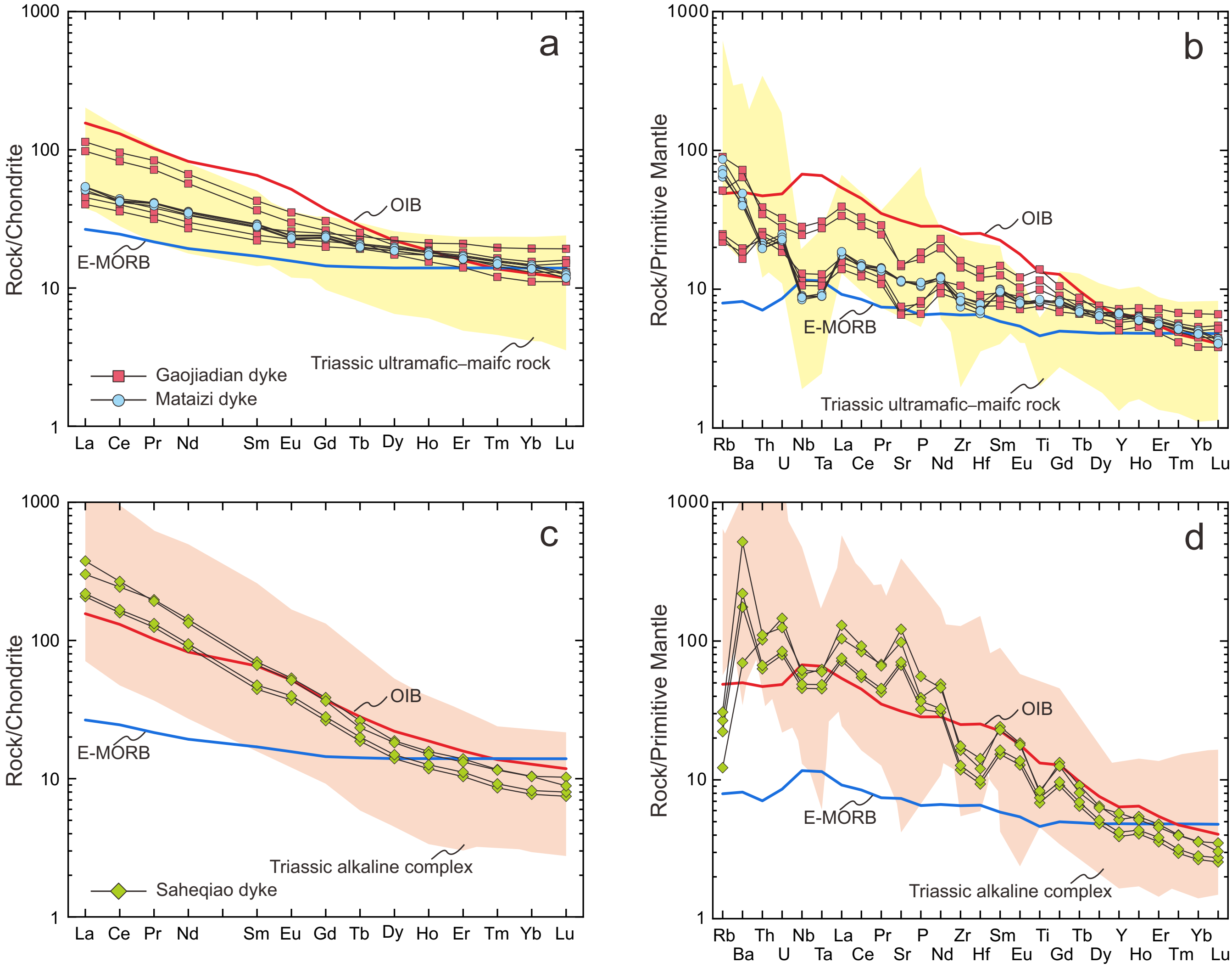

a
Rock/Chondrite
1000
100
10
1
La Ce Pr Nd Sm Eu Gd Tb Dy Ho Er Tm Yb Lu
OIB
E-MORB
Triassic ultramafic–maifc rock
Gaojiadian dyke
Mataizi dyke
b
Rock/Primitive Mantle
Rb Ba Th U Nb Ta La Ce Pr Sr P Nd Zr Hf Sm Eu Ti Gd Tb Dy Y Ho Er Tm Yb Lu
OIB
E-MORB
Triassic ultramafic–maifc rock
c
Rock/Chondrite
OIB
E-MORB
Triassic alkaline complex
Saheqiao dyke
d
Rock/Primitive Mantle
OIB
E-MORB
Triassic alkaline complex

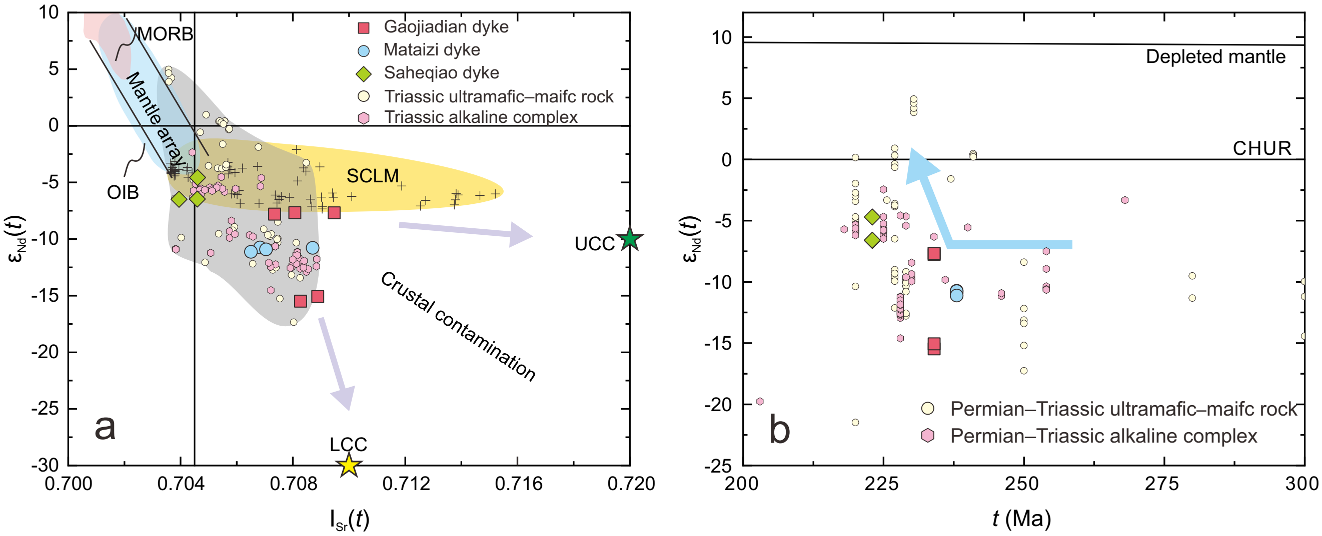

MORB
Mantle array
OIB
SCLM
UCC
LCC
Crustal contamination
Gaojiadian dyke
Mataizi dyke
Saheqiao dyke
Triassic ultramafic–maifc rock
Triassic alkaline complex
a
$\varepsilon_{Nd}(t)$
$I_{Sr}(t)$
Depleted mantle
CHUR
Permian–Triassic ultramafic–maifc rock
Permian–Triassic alkaline complex
b
t (Ma)

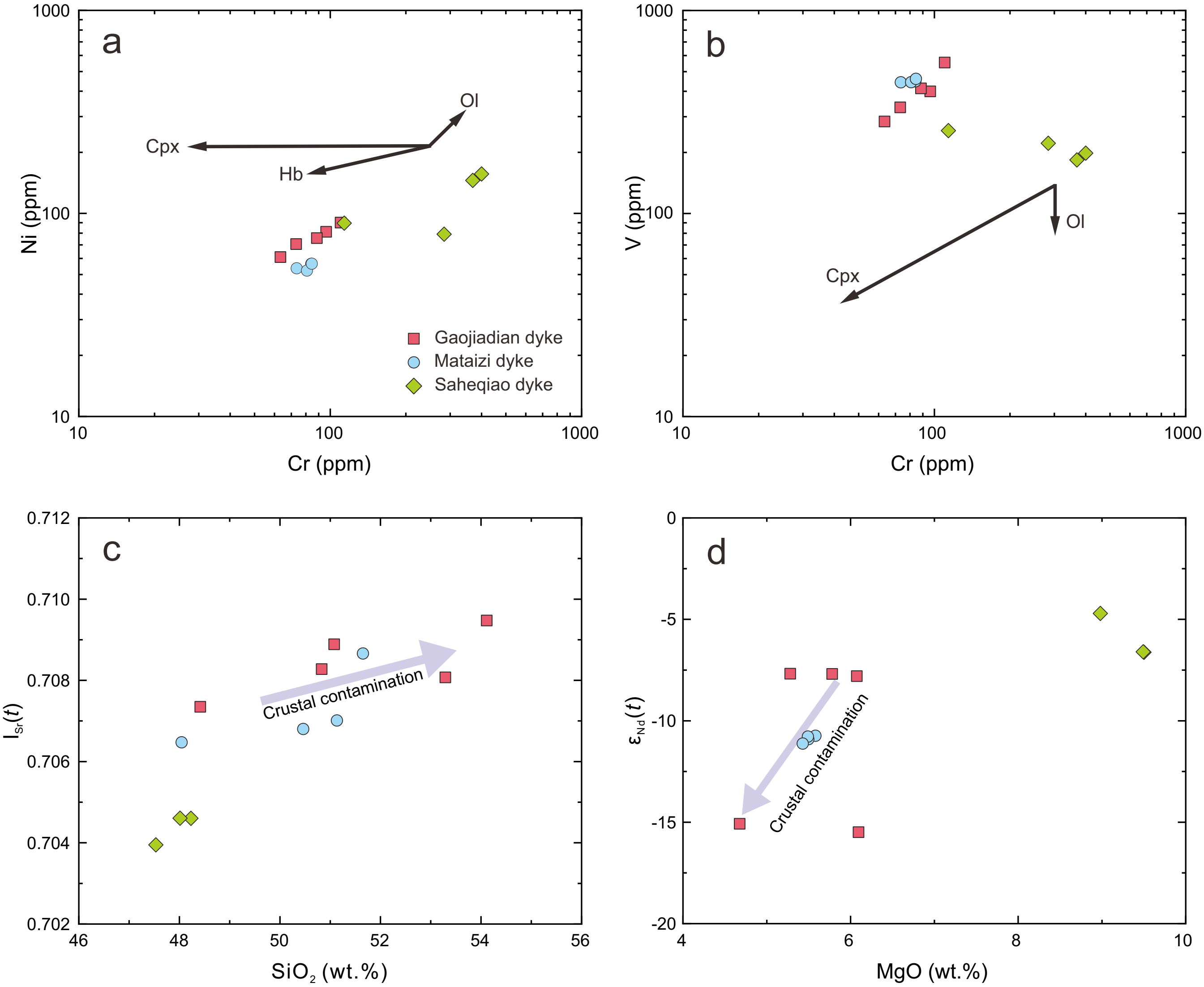

a
Ol
Cpx
Hb
Ni (ppm)
Cr (ppm)
Gaojiadian dyke
Mataizi dyke
Saheqiao dyke
b
V (ppm)
Cr (ppm)
Cpx
Ol
c
Crustal contamination
$I_{Sr}(t)$
SiO_2 (wt.%)
d
Crustal contamination
$\varepsilon_{Nd}(t)$
MgO (wt.%)

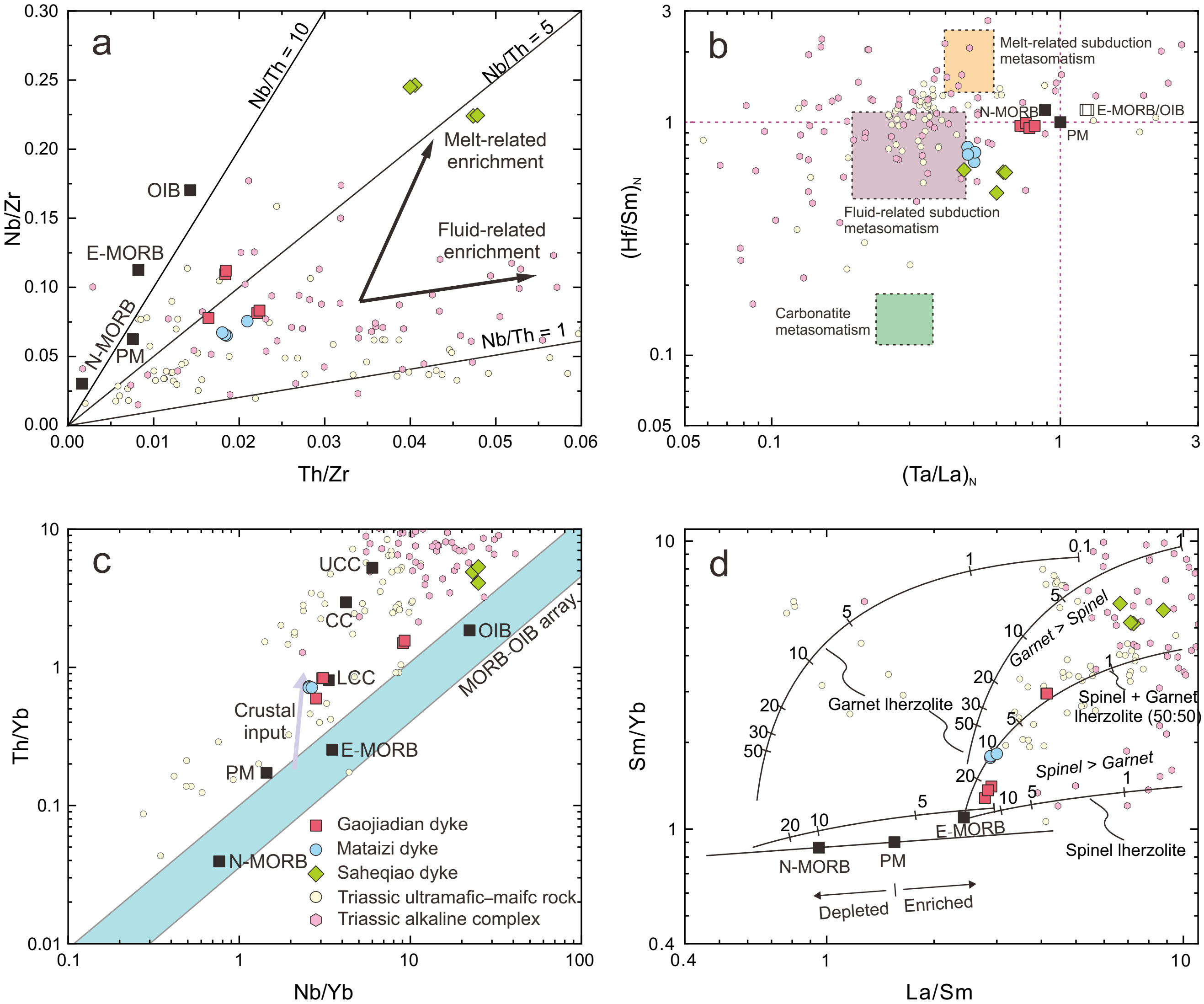

a
Nb/Th = 10
Nb/Th = 5
Nb/Th = 1
Melt-related enrichment
Fluid-related enrichment
OIB
E-MORB
N-MORB
PM
Nb/Zr
Th/Zr
b
Melt-related subduction metasomatism
N-MORB
E-MORB/OIB
PM
Fluid-related subduction metasomatism
Carbonatite metasomatism
(Hf/Sm)N
(Ta/La)N
c
UCC
CC
LCC
OIB
MORB-OIB array
Crustal input
PM
E-MORB
N-MORB
Gaojiadian dyke
Mataizi dyke
Saheqiao dyke
Triassic ultramafic–maifc rock
Triassic alkaline complex
Th/Yb
Nb/Yb
d
Garnet lherzolite
Garnet > Spinel
Spinel + Garnet lherzolite (50:50)
Spinel > Garnet
Spinel lherzolite
E-MORB
N-MORB
PM
Depleted
Enriched
Sm/Yb
La/Sm

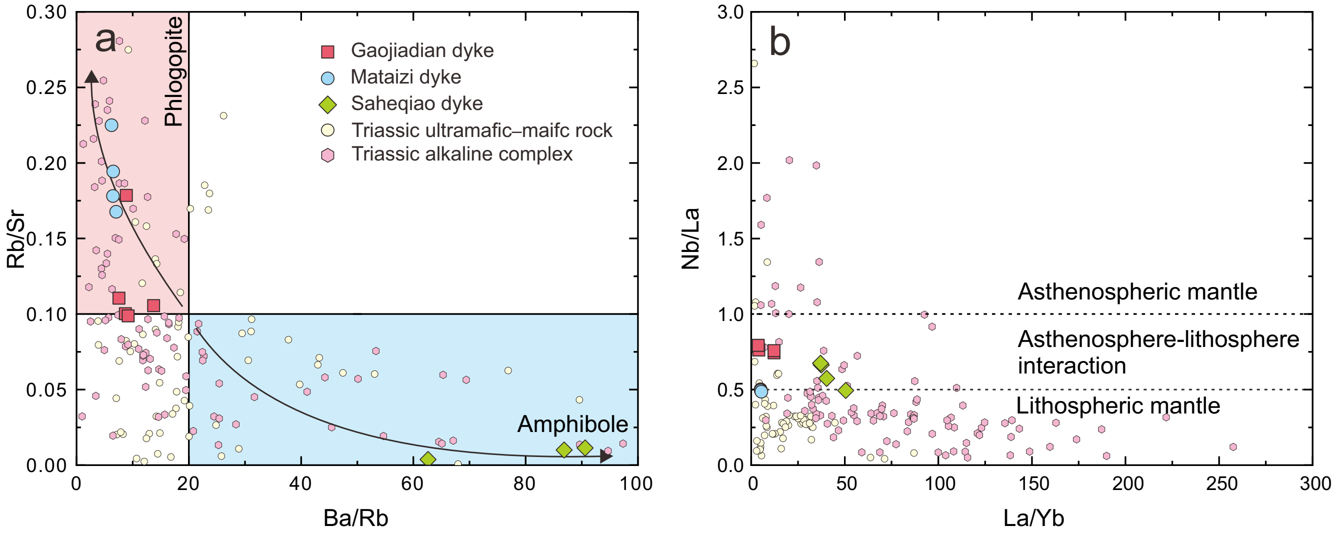
a
Phlogopite
Amphibole
Gaojiadian dyke
Mataizi dyke
Saheqiao dyke
Triassic ultramafic–maifc rock
Triassic alkaline complex
Rb/Sr
Ba/Rb
b
Asthenospheric mantle
Asthenosphere-lithosphere interaction
Lithospheric mantle
Nb/La
La/Yb

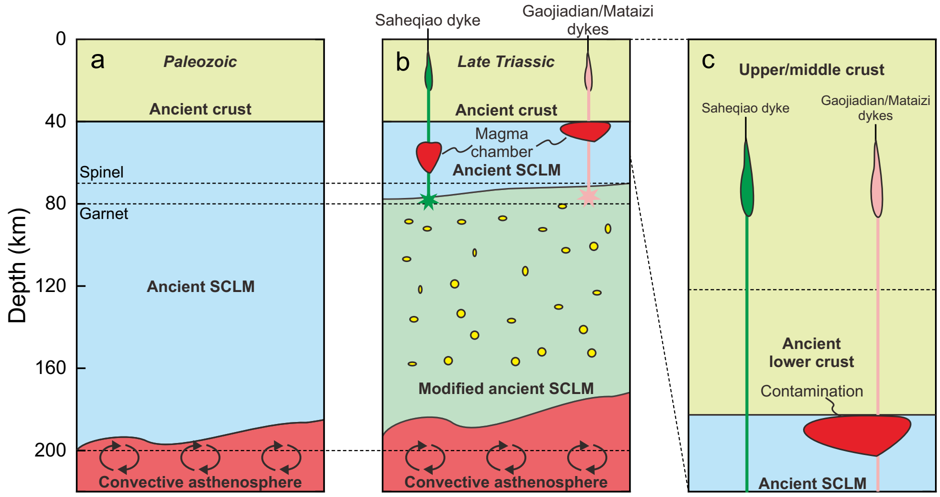

Depth (km)
0
40
80
120
160
200
a
Paleozoic
Ancient crust
Spinel
Garnet
Ancient SCLM
Convective asthenosphere
Saheqiao dyke
Gaojiadian/Mataizi dykes
b
Late Triassic
Ancient crust
Magma chamber
Ancient SCLM
Modified ancient SCLM
Convective asthenosphere
c
Upper/middle crust
Saheqiao dyke
Gaojiadian/Mataizi dykes
Ancient lower crust
Contamination
Ancient SCLM

Lithospheric modification at the onset of the destruction of the North China Craton: evidence from Late Triassic mafic dykes

Wang et al.

Supplementary Material

The Supplementary Material includes:

- Analytical methods
- Fig. S1
- Table S1–9

Analytical methods

In situ zircon U-Pb dating

Zircon grains were extracted from crushed samples by standard heavy-liquid and magnetic techniques, and purified by hand-picking under a binocular microscope. The selected grains were mounted in epoxy resin and polished down to about half their thickness to expose the grain interiors, and then imaged under reflected and transmitted light and by Cathodoluminescence (CL). The CL images were acquired using a cathodoluminescent spectrometer (Garton Mono CL3+) attached to a Quanta 200F ESEM at Peking University.

Measurements of zircon U, Th and Pb isotopes on samples J1416 and 15SHQ05 were conducted using a CAMECA IMS-1280 secondary ion mass spectrometry (SIMS) at the Institute of Geology and Geophysics, Chinese Academy of Sciences, following the standard procedures described in Li et al. (2009). The primary O^{2-} ion beam spot is about 20×30 μm in size. Analyses of the standard zircon Plešovice were interspersed with unknown grains. Pb/U calibration was performed relative to zircon standard Plešovice (Sláma et al., 2008); U and Th concentrations were calibrated against zircon standard 91500 (Wiedenbeck et al., 1995). In order to monitor the external uncertainties of SIMS U-Pb zircon dating calibrated against Plešovice standard, an in-house zircon standard Qinghu was alternately analyzed as an unknown together with other unknown zircons. Nine measurements on Qinghu zircon yield a concordia age of 160.0 ± 1.6 Ma (2*s*), which is identical within error with the recommended value of 159.5 ± 0.2 Ma (Li et al., 2013). A long-term uncertainty of 1.5% (1 relative standard deviation) for $^{206}Pb/^{238}U$ measurements of the standard zircons was propagated to the unknowns. Measured compositions were corrected for common Pb using non-radiogenic ^{204}Pb. Corrections are sufficiently small to be insensitive to the choice of common Pb composition, and an average of present-day crustal composition (Stacey and Kramers, 1975) is used for the common Pb assuming that the common Pb is largely surface contamination introduced during sample preparation. Measurements of U, Th and Pb in zircons from sample 18NC51 were carried out on an Agilent-7500a quadrupole inductively coupled plasma mass spectrometer coupled with a New Wave UP-193 solid-state laser-ablation system (LA-ICPMS) in the Geological Lab Center, China University of Geosciences, Beijing (CUGB), following the analytical procedures described in Song et al. (2010a). Laser spot size of 36 μm, laser energy density of 8.5 J/cm^2 and a repetition rate of 10 Hz were applied for analysis. The ablated sample material was carried into the ICP-MS by high-purity Helium gas. NIST 610 glass and Harvard standard zircon 91500 (Wiedenbeck et al., 1995) were used as external standards, Si as the internal standard and the standard zircon Qinghu as secondary standard. Five measurements on Qinghu zircon yield a concordia age of 160.9 ± 2.5 Ma (2*s*), which is identical within error with the recommended value of 159.5 ± 0.2 Ma (Li et al., 2013). The software GLITTER (ver. 4.4, Macquarie University) was used for data reduction. The common lead correction was done following Andersen (2002). Age calculations and plots of concordia diagrams were made using Isoplot (ver. 3.0) (Ludwig, 2003).

Mineral Chemistry

Mineral chemistry was collected using a JEOL 8230 electron probe micro analyzer (EPMA) at the MOE Key Laboratory of Orogenic Belts and Crustal Evolution, Peking University, following analytical procedures described in Li et al. (2018). The EPMA is equipped with four spectrometers (CH1–CH4). The PETJ crystal (CH1) has been used for K, Ca and Ti, the two TAP crystals (CH2, CH4) for Na, Si, Mg and Al and the LIFH crystal (CH3) for Cr, Mn, Fe and Ni. For all elements, the Ka line has been utilized. The acceleration voltage and the beam current were 15 kV with 10 nA, respectively. The beam was set to diameters of 1–2 μm, and counting times were 10–15 s. The SPI 53 minerals standard (U.S.) was utilized for the quantitative analysis: sanidine was employed for K; diopside for Ca and Mg; rutile for Ti; jadeite for Na, Al and Si; chromium oxide for Cr; rhodonite for Mn; hematite for Fe; and nickel silicide for Ni. At the final calibration stage, the PRZ correction was performed. Analytical precision is better than 0.02% for most oxides. The mineral formulae were calculated with the program AX (Holland, 2009) and given for fixed oxygen values with Fe^{3+} calculated by stoichiometric charge balance.

Bulk-rock major and trace element analyses

All the samples are fresh cuttings away from late veinlets, with any surface contaminants trimmed off before being thoroughly cleaned. Fresh portions of the trimmed samples were crushed into 1–2 cm size chips using a percussion mill. These rock fragments were ultrasonically cleaned in Milli-Q water, dried and powdered in a thoroughly cleaned agate mill to 200 mesh in the clean laboratory at the Langfang Regional Geological Survey, China. Bulk-rock major and trace element analyses were undertaken in the Geological Lab Center, CUGB following the procedures described in Song et al. (2010b). Major elements were analyzed on a Leeman Prodigy inductively coupled plasma-optical emission spectrometer (ICP-OES) system with high dispersion Echelle optics. Based on rock standards AGV-2, BHVO-2 (US Geological Survey: USGS) and GSR-3 (national geological standard reference material of China), the analytical precisions (1*s*) for most major element oxides are better than 1% with the exception of TiO_2 (~1.5%) and P_2O_5 (~2.0%) (Table S8). Loss on ignition (LOI) was determined by placing 1 g of sample in the furnace at 1000 ℃ for a few hours and then reweighting the cooled samples.

Bulk-rock trace elements were analyzed using an Agilent-7500a quadrupole inductively coupled plasma mass spectrometer (ICPMS). About 35 mg powder of each sample was dissolved in distilled acid mixture (1:1 HF + HNO_3) with Teflon digesting vessels and heated on a hot-plate at 195 ℃ for 48 hours using high-pressure bombs for digestion/dissolution. The sample was then evaporated to incipient dryness, refluxed with 1 mL of 6 N HNO_3 and heated again to incipient dryness. The sample was again dissolved in 2 mL of 3 N HNO_3 and heated at 165 ℃ for further 24 hours to guarantee complete digestion/dissolution. The sample was finally diluted with Milli-Q water to a dilution factor of 2000 in 2% HNO_3 solution for ICPMS analyses. Rock standards AGV-2, W-2 (USGS) and GSR-3 (national geological standard reference material of China) were used to monitor the analytical accuracy and precision. Analytical accuracy, as indicated by relative difference between measured and recommended values is better than 5% for most elements, and 10 ~ 15% for Cu, Zn, Gd, and Ta (Table S9).

Bulk-rock Sr-Nd isotope analyses

Separation and purification of Sr and Nd were done using conventional two-column ion exchange procedures in the ultraclean laboratory of the MOE Key Laboratory at Peking University. Approximately 250 mg powder of each sample was dissolved with distilled acid mixture (HF + $HClO_4$) in a sealed Savillex beaker on a hot-plate for 168 hours. The ion exchange procedures include (1) a separation of Sr and a group separation of light REE through a cation-exchange column (1×7.5 cm^2, packed with 200 mesh AG50W resin); and (2) a purification of Nd through a second cation-exchange column (0.5×5.5 cm^2, packed with 200 mesh P507 resin), conditioned and cleaned with dilute HCl. Sr-Nd isotopic ratios were measured using a Thermo-Finnigan Triton thermal ionization mass spectrometer (TIMS) at the Isotope Laboratory of the Tianjin Institute of Geology and Mineral Resources. The $^{87}Rb/^{86}Sr$ and $^{147}Sm/^{144}Nd$ ratios were calculated using ICP-MS analyzed Sm and Nd concentrations. Mass fractionation was corrected by normalizing the measured $^{87}Sr/^{86}Sr$ and $^{143}Nd/^{144}Nd$ against $^{86}Sr/^{88}Sr$ ratio of 0.1194 and $^{146}Nd/^{144}Nd$ ratio of 0.7219, respectively. Rock standard USGS BCR-2 was used to evaluate the separation and purification process of Sr and Nd, which yielded weighted mean $^{87}Sr/^{86}Sr$ ratio of 0.705005 ± 10 (2SE) and $^{143}Nd/^{144}Nd$ ratio of 0.512640 ± 10 (2SE). In order to monitor the data quality during the period of data acquisition, NBS-987 Sr standard and LRIG Nd standard was analyzed and gave weighted mean $^{87}Sr/^{86}Sr$ ratio of 0.710269 ± 10 (2SE) and $^{143}Nd/^{144}Nd$ ratio of 0.512204 ± 16 (2SE).

References

Andersen, T., 2002. Correction of common lead in U–Pb analyses that do not report 204Pb. Chemical Geology 192, 59-79.

Holland, T. J. B., 2009. AX: a program to calculate activities of mineral end-members from chemical analyses. Available at: http://128.40.77.191/ccp/web-mirrors/crush/astaff/holland/ax.html.

Li, X.-H., Liu, Y., Li, Q.-L., Guo, C.-H., Chamberlain, K.R., 2009. Precise determination of Phanerozoic zircon Pb/Pb age by multicollector SIMS without external standardization. Geochemistry, Geophysics, Geosystems 10, Q04010.

Li, X.-H., Tang, G., Gong, B., Yang, Y., Hou, K., Hu, Z., Li, Q., Liu, Y., Li, W., 2013. Qinghu zircon: A working reference for microbeam analysis of U-Pb age and Hf and O isotopes. Chinese Science Bulletin 58, 4647-4654.

Li, X., Zhang, L., Wei, C., Slabunov, A.I., Bader, T., 2018. Quartz and orthopyroxene exsolution lamellae in clinopyroxene and the metamorphicP-Tpath of Belomorian eclogites. Journal of Metamorphic Geology 36, 1-22.

Ludwig, K.R., 2003. User's manual for Isoplot 3.0: A geochronological toolkit for Microsoft Excel. Berkeley Geochronology Centre, Special Publication.

Putirka, K.D., 2008. Thermometers and barometers for volcanic systems. Reviews in Mineralogy and Geochemistry 69, 61-120.

Sláma, J., Košler, J., Condon, D.J., Crowley, J.L., Gerdes, A., Hanchar, J.M., Horstwood, M.S., Morris, G.A., Nasdala, L., Norberg, N., 2008. Plešovice zircon—a new natural reference material for U–Pb and Hf isotopic microanalysis. Chemical Geology 249, 1-35.

Song, S.G., Niu, Y.L., Wei, C.J., Ji, J.Q., Su, L., 2010a. Metamorphism, anatexis, zircon ages and tectonic evolution of the Gongshan block in the northern Indochina continent—An eastern extension of the Lhasa Block. Lithos 120, 327-346.

Song, S.G., Su, L., Li, X.H., Zhang, G.B., Niu, Y.L., Zhang, L.F., 2010b. Tracing the 850-Ma continental flood basalts from a piece of subducted continental crust in the North Qaidam UHPM belt, NW China. Precambrian Research 183, 805-816.

Stacey, J.S., Kramers, J.D., 1975. Approximation of terrestrial lead isotope evolution by a two-stage model. Earth and Planetary Science Letters 26, 207-221.

Sun, S.S., McDonough, W.F., 1989. Chemical and isotopic systematics of oceanic basalts: implications for mantle composition and processes. Geological Society, London, Special Publications 42, 313-345.

Wiedenbeck, M., Allé, P., Corfu, F., Griffin, W.L., Meier, M., Oberli, F., Quadt, A.V., Roddick, J.C., Spiegel, W., 1995. Three natural zircon standards for U-Th-Pb, Lu-Hf, trace element and REE analyses. Geostandards Newsletter 19, 1-23.

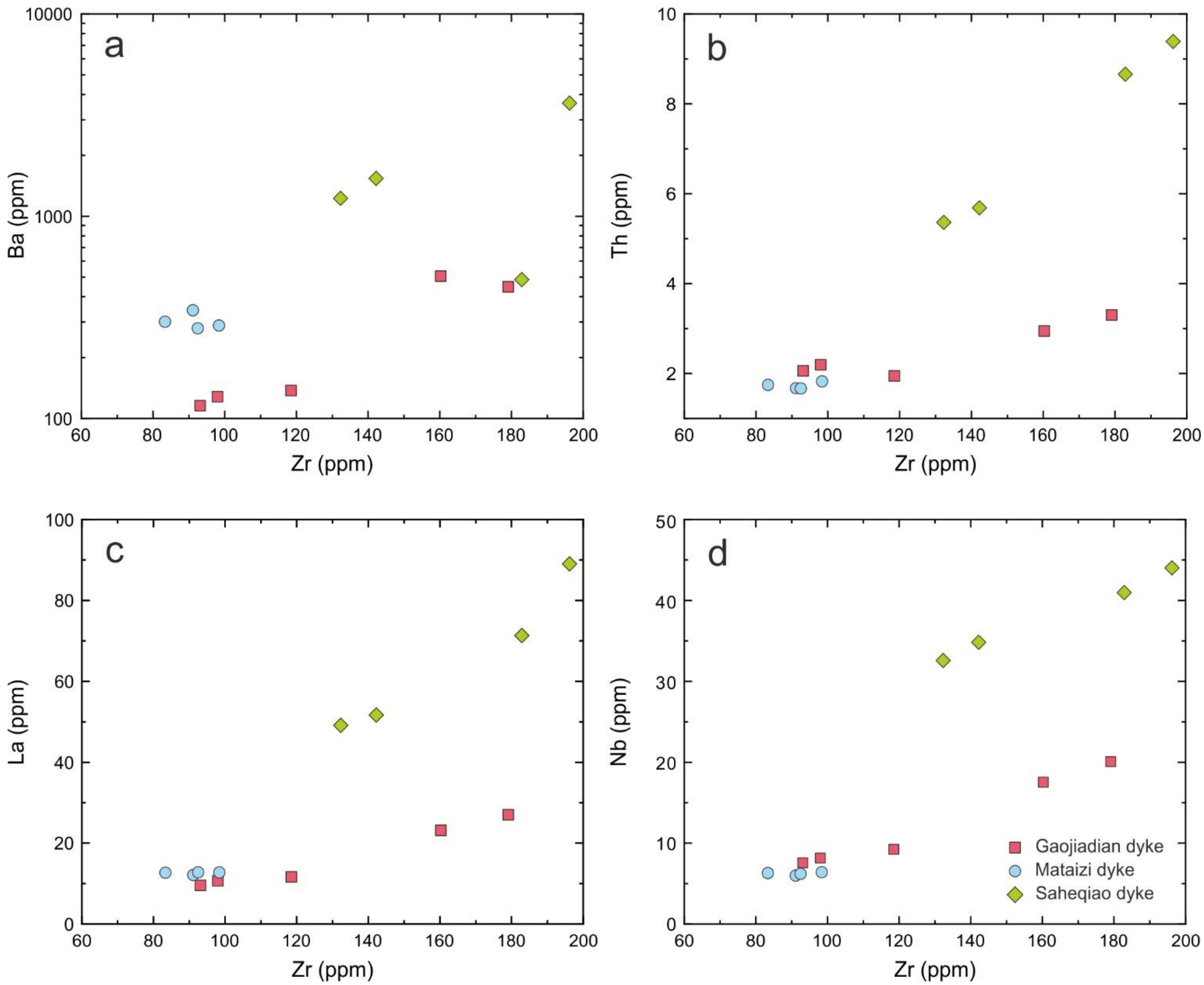

Fig. S1 Co-variation diagrams of (a) Ba-Zr, (b) Th-Zr, (c) La-Zr, and (d) Nb-Zr for the Late Triassic mafic dykes in Eastern Hebei.

Table S1 *In situ* SIMS zircon U-Pb data for the Late Triassic Gaojiadian and Saheqiao mafic dykes in Eastern Hebei and the standard used during analyses.

Spot	Contents (ppm)			Th/U	Isotopic ratios (^{204}Pb-corrected)						Isotopic ages (Ma) (^{204}Pb-corrected)						Disc.[a]
	Pb	U	Th	(Meas.)	$^{207}Pb/^{206}Pb$	1*s*(%)	$^{207}Pb/^{235}U$	1*s*(%)	$^{206}Pb/^{238}U$	1*s*(%)	$^{207}Pb/^{206}Pb$	1*s*	$^{207}Pb/^{235}U$	1*s*	$^{206}Pb/^{238}U$	1*s*	(%)
Gaojiadian dyke J1416																	
1-1	10	251	221	0.88	0.0502	1.01	0.2573	1.90	0.0371	1.61	205	23	232	4	235	4	-1
1-2	14	344	472	1.37	0.0487	2.03	0.2501	2.53	0.0372	1.51	134	47	227	5	236	3	-4
1-3	14	354	325	0.92	0.0510	0.75	0.2587	1.68	0.0368	1.51	240	17	234	4	233	3	0
1-4	4	109	67	0.62	0.0501	1.84	0.2556	2.38	0.0370	1.52	202	42	231	5	234	3	-1
1-5	8	205	132	0.64	0.0508	1.00	0.2536	1.87	0.0362	1.58	232	23	230	4	229	4	0
1-6	9	233	215	0.92	0.0502	1.26	0.2536	1.97	0.0366	1.52	204	29	229	4	232	3	-1
1-7	6	154	151	0.98	0.0515	1.42	0.2670	2.21	0.0376	1.68	264	32	240	5	238	4	1
1-8	6	142	97	0.68	0.0498	1.58	0.2582	2.18	0.0376	1.50	185	36	233	5	238	4	-2
1-9	9	221	169	0.77	0.0502	1.32	0.2548	2.00	0.0368	1.50	206	30	230	4	233	3	-1
1-10	3	74	48	0.64	0.0498	3.64	0.2474	3.94	0.0360	1.52	188	83	224	8	228	3	-2
1-11	6	154	99	0.64	0.0497	1.80	0.2455	2.35	0.0358	1.51	182	41	223	5	227	3	-2
1-12	4	96	65	0.68	0.0498	2.44	0.2553	2.99	0.0372	1.73	187	56	231	6	235	4	-2
1-13	7	168	117	0.70	0.0517	1.61	0.2659	2.21	0.0373	1.52	271	36	239	5	236	4	1
1-14	8	190	173	0.91	0.0503	1.27	0.2649	2.16	0.0382	1.75	207	29	239	5	242	4	-1
1-15	6	146	105	0.72	0.0517	1.14	0.2694	1.92	0.0378	1.55	274	26	242	4	239	4	1
1-16	3	81	51	0.63	0.0524	1.51	0.2691	2.17	0.0373	1.55	302	34	242	5	236	4	3
1-17	6	146	103	0.71	0.0513	1.47	0.2585	2.10	0.0366	1.50	254	34	233	4	231	3	1
1-18	7	185	135	0.73	0.0502	1.23	0.2544	1.95	0.0368	1.51	205	28	230	4	233	3	-1
1-19	8	183	137	0.75	0.0513	1.04	0.2656	1.84	0.0375	1.52	255	24	239	4	237	4	1
Saheqiao dyke 15SHQ05																	
2-3	84	2067	781	0.38	0.0525	1.40	0.2481	2.06	0.0343	1.50	306	32	225	4	217	3	4
2-5	18	436	209	0.48	0.0466	6.80	0.2250	6.96	0.0350	1.51	28	155	206	13	222	3	-7
2-6	15	387	59	0.15	0.0515	3.15	0.2524	3.52	0.0356	1.57	262	71	229	7	225	3	1
2-7	46	1139	332	0.29	0.0504	0.84	0.2436	1.72	0.0351	1.50	213	19	221	3	222	3	0
2-8	113	2601	1544	0.59	0.0504	0.70	0.2437	1.66	0.0351	1.50	213	16	221	3	222	3	0
2-9	19	468	196	0.42	0.0505	1.26	0.2442	1.96	0.0351	1.50	217	29	222	4	222	3	0
2-10	166	3533	2883	0.82	0.0507	1.50	0.2507	2.13	0.0359	1.51	225	34	227	4	227	3	0

2-14	14	306	251	0.82	0.0506	1.88	0.2472	2.63	0.0354	1.84	222	43	224	5	225	4	0
2-15	26	549	425	0.78	0.0490	1.19	0.2461	1.95	0.0365	1.54	147	28	223	4	231	3	-3
2-16	42	981	473	0.48	0.0502	1.26	0.2450	1.99	0.0354	1.54	204	29	222	4	224	3	-1
2-17	30	660	562	0.85	0.0502	3.02	0.2424	3.38	0.0350	1.51	206	69	220	7	222	3	-1
Standard Qinghu																	
1	30	937	592	0.63	0.0495	1.64	0.1739	2.24	0.0255	1.52	173	38	163	3	162	2	0
2	51	1873	375	0.20	0.0488	1.25	0.1673	1.95	0.0249	1.50	136	29	157	3	158	2	-1
3	26	833	518	0.62	0.0491	1.12	0.1706	1.97	0.0252	1.62	150	26	160	3	161	3	0
4	39	1310	582	0.44	0.0492	0.94	0.1702	1.78	0.0251	1.51	159	22	160	3	160	2	0
5	20	640	360	0.56	0.0480	1.30	0.1661	1.99	0.0251	1.51	100	30	156	3	160	2	-2
6	20	656	348	0.53	0.0484	1.47	0.1669	2.15	0.0250	1.57	120	34	157	3	159	2	-2
7	57	1811	1065	0.59	0.0500	1.04	0.1743	1.89	0.0253	1.58	196	24	163	3	161	3	1
8	46	1507	729	0.48	0.0496	0.88	0.1732	1.74	0.0253	1.50	177	20	162	3	161	2	1
9	19	651	208	0.32	0.0494	1.31	0.1702	2.01	0.0250	1.53	168	30	160	3	159	2	0

a: Disc. = Discordance

Table S2 *In situ* LA-ICPMS zircon U-Pb data for the Late Triassic Mataizi mafic dyke in Eastern Hebei and the standard used during analyses.

Spot	Contents (ppm)			Th/U	Isotopic ratios (Corrected)						Isotopic ages (Ma) (Corrected)						Disc.[a]
	Pb	U	Th		$^{207}Pb/^{206}Pb$	1*s*	$^{207}Pb/^{235}U$	1*s*	$^{206}Pb/^{238}U$	1*s*	$^{207}Pb/^{206}Pb$	1*s*	$^{207}Pb/^{235}U$	1*s*	$^{206}Pb/^{238}U$	1*s*	(%)
Mataizi dyke 18NC51																	
3-1	37	878	155	0.18	0.05077	0.00158	0.25768	0.00834	0.03680	0.00060	230	45	233	7	233	4	0
3-2	61	77	130	1.69	0.16904	0.00397	11.24605	0.28349	0.48243	0.00806	2548	21	2544	24	2538	35	0
3-3	110	158	142	0.90	0.17140	0.00371	11.51027	0.27293	0.48696	0.00787	2571	20	2565	22	2558	34	1
3-4	181	275	127	0.46	0.17338	0.00360	11.77358	0.27102	0.49240	0.00782	2591	19	2587	22	2581	34	0
3-5	142	227	101	0.45	0.16661	0.00346	10.96456	0.25234	0.47721	0.00757	2524	19	2520	21	2515	33	0
3-6	160	204	166	0.82	0.19942	0.00412	14.94907	0.34270	0.54358	0.00863	2821	18	2812	22	2798	36	1
3-7	82	122	87	0.71	0.16972	0.00370	11.28668	0.26929	0.48223	0.00780	2555	20	2547	22	2537	34	1
3-8	100	140	143	1.02	0.16879	0.00375	11.27217	0.27295	0.48424	0.00790	2546	20	2546	23	2546	34	0
3-9	38	59	30	0.51	0.16942	0.00417	11.27493	0.29532	0.48256	0.00818	2552	23	2546	24	2538	36	1
3-10	79	118	58	0.50	0.17515	0.00384	12.03007	0.28835	0.49804	0.00806	2607	20	2607	22	2605	35	0
3-11	68	92	115	1.25	0.16829	0.00397	11.19244	0.28349	0.48225	0.00805	2541	22	2539	24	2537	35	0
3-12	15	307	162	0.53	0.05141	0.00298	0.27448	0.01591	0.03872	0.00073	259	98	246	13	245	5	0
3-13	96	133	134	1.01	0.17382	0.00382	11.75060	0.28253	0.49018	0.00793	2595	20	2585	22	2571	34	1
Standard Qinghu																	
1					0.04911	0.00182	0.16931	0.00631	0.02501	0.00040	153	57	159	5	159	3	0
2					0.04998	0.00176	0.17261	0.00622	0.02504	0.00041	194	53	162	5	159	3	2
3					0.04923	0.00181	0.17344	0.00664	0.02553	0.00044	159	57	162	6	163	3	-1
4					0.04913	0.00191	0.17021	0.00709	0.02512	0.00047	154	63	160	6	160	3	0
5					0.04939	0.00229	0.17677	0.00893	0.02598	0.00053	166	79	165	8	165	3	0

a: Disc. = Discordance

Table S3 Representative analyses of clinopyroxene for the Late Triassic Gaojiadian mafic dyke in Eastern Hebei.

No.	J1416-2	J1416-3	J1416-4	J1416-7	J1416-8	J1416-9	J1416-11	J1416-15
SiO_2	52.37	51.89	51.25	51.70	51.26	50.24	51.34	50.83
TiO_2	0.44	0.45	0.42	0.48	0.55	0.70	0.45	0.47
Al_2O_3	2.01	2.19	2.68	1.89	1.99	2.09	2.59	2.17
Cr_2O_3	0.08	0.06	0.05	0.12	0.11	0.06	0.06	0.12
FeO^T	12.14	14.12	13.41	13.86	14.56	16.71	12.81	13.04
MnO	0.24	0.29	0.23	0.28	0.28	0.31	0.30	0.32
MgO	16.36	16.08	15.41	15.42	14.33	12.47	15.88	15.29
CaO	17.31	15.73	16.60	16.13	17.70	17.45	16.10	17.44
Na_2O	0.19	0.23	0.29	0.25	0.14	0.24	0.28	0.21
K_2O	bdl[a]	bdl	0.01	0.02	0.01	bdl	bdl	0.02
Total	101.14	101.04	100.35	100.15	100.93	100.27	99.81	99.91
# of O	6	6	6	6	6	6	6	6
Si	1.93	1.92	1.91	1.93	1.91	1.91	1.92	1.90
Ti	0.01	0.01	0.01	0.01	0.02	0.02	0.01	0.01
Al^{IV}	0.07	0.08	0.09	0.07	0.09	0.09	0.08	0.10
Al^{VI}	0.01	0.01	0.03	0.02	_	_	0.03	_
Cr	_	_	_	_	_	_	_	_
Fe^{3+}	0.05	0.06	0.07	0.04	0.06	0.06	0.05	0.09
Fe^{2+}	0.33	0.38	0.35	0.39	0.39	0.47	0.35	0.32
Mn	0.01	0.01	0.01	0.01	0.01	0.01	0.01	0.01
Mg	0.90	0.89	0.86	0.86	0.80	0.71	0.88	0.85
Ca	0.68	0.62	0.66	0.65	0.71	0.71	0.64	0.70
Na	0.01	0.02	0.02	0.02	0.01	0.02	0.02	0.02
K	_	_	_	_	_	_	_	_
Wo	0.34	0.31	0.32	0.32	0.35	0.35	0.32	0.34
En	0.44	0.44	0.42	0.43	0.39	0.35	0.43	0.42
Fs	0.16	0.19	0.17	0.20	0.19	0.23	0.17	0.16
Jd	0.01	0.01	0.02	0.02	_	_	0.03	_

Ae	0.05	0.06	0.06	0.04	0.06	0.06	0.05	0.08
X_{Mg}[b]	0.73	0.70	0.71	0.69	0.67	0.60	0.72	0.73
P (kbar)[c]	2.5	3.8	4.7	3.3	2.1	2.9	4.4	2.9
T (℃)[c]	1163	1162	1174	1164	1127	1116	1178	1146

a: bdl: below detection limit.
b: X_{Mg} = Mg/(Mg + Fe^{2+}).
c: Cystallization conditions calculated using the clinopyroxene-liquid thermometer of Putirka (2008).

Table S4 Representative analyses of plagioclase for the Late Triassic mafic dykes in Eastern Hebei.

No.	J1416-2	J1416-3	J1416-5	J1416-6	J1416-13	15SHQ03-2	15SHQ03-14	15SHQ03-15	15SHQ03-16
Sample	Gaojiadian dyke					Saheqiao dyke			
SiO_2	56.90	53.63	54.05	53.24	52.52	70.73	68.12	70.58	68.70
TiO_2	0.01	0.02	0.05	0.02	0.03	0.00	0.01	0.05	0.03
Al_2O_3	27.31	29.84	27.70	29.30	30.25	20.28	20.16	20.77	20.36
Cr_2O_3	bdl[a]	bdl	bdl	bdl	0.01	0.03	0.01	0.01	bdl
FeO^T	0.57	0.58	0.64	0.74	0.60	0.08	0.38	0.07	0.12
MnO	bdl	0.01	0.04	0.03	0.02	bdl	bdl	0.02	0.01
MgO	0.04	0.05	0.07	0.07	0.07	bdl	0.10	bdl	0.07
CaO	10.05	13.05	11.72	13.15	13.97	0.10	0.42	0.39	0.13
Na_2O	5.78	4.16	4.87	4.18	3.83	9.60	10.04	9.29	8.85
K_2O	0.16	0.20	0.24	0.31	0.10	0.03	0.39	0.09	0.33
Total	100.82	101.54	99.38	101.04	101.40	100.85	99.63	101.27	98.60
# of O	8	8	8	8	8	8	8	8	8
Si	2.54	2.40	2.46	2.40	2.36	3.03	2.98	3.01	3.01
Ti	–	–	–	–	–	–	–	–	–
Al	1.44	1.57	1.49	1.56	1.60	1.02	1.04	1.04	1.05
Cr	–	–	–	–	–	–	–	–	–
Fe^{3+}	0.02	0.02	0.02	0.03	0.02	–	0.01	–	–
Fe^{2+}	–	–	–	–	–	–	–	–	–
Mn	–	–	–	–	–	–	–	–	–
Mg	–	–	0.01	0.01	0.01	–	0.01	–	0.01
Ca	0.48	0.63	0.57	0.63	0.67	0.01	0.02	0.02	0.01
Na	0.50	0.36	0.43	0.37	0.33	0.80	0.85	0.77	0.75
K	0.01	0.01	0.01	0.02	0.01	–	0.02	0.01	0.02
X_{An}	0.49	0.63	0.56	0.62	0.66	0.01	0.02	0.02	0.01
X_{Ab}	0.51	0.36	0.42	0.36	0.33	0.99	0.95	0.97	0.97
X_{Or}	0.01	0.01	0.01	0.02	0.01	0.00	0.02	0.01	0.02

a: bdl: below detection limit.

Table S5 Representative analyses of hornblende for the Late Triassic Saheqiao mafic dyke in Eastern Hebei.

No.	15SHQ03-2	15SHQ03-3	15SHQ03-5	15SHQ03-8	15SHQ03-10	15SHQ03-13	15SHQ03-15	15SHQ03-16
SiO_2	39.00	39.34	38.72	38.70	39.56	39.44	39.75	39.23
TiO_2	3.21	2.93	3.10	4.07	3.43	4.15	3.57	3.17
Al_2O_3	14.04	14.17	14.38	14.72	14.21	14.60	13.84	13.97
Cr_2O_3	bdl[a]	0.01	bdl	0.01	bdl	bdl	0.07	bdl
FeO^T	13.33	12.88	13.76	11.33	11.28	10.09	10.56	12.22
MnO	0.22	0.16	0.28	0.07	0.13	0.10	0.11	0.16
MgO	11.67	11.87	11.44	12.50	13.21	13.52	13.38	12.71
CaO	12.49	12.71	12.63	12.37	12.88	12.82	12.77	12.33
Na_2O	2.37	2.42	2.42	2.31	2.21	2.06	2.18	2.35
K_2O	1.07	0.96	1.07	1.28	1.19	1.01	1.10	1.13
Total	97.40	97.45	97.80	97.36	98.10	97.79	97.33	97.27
# of O	23	23	23	23	23	23	23	23
Si	5.84	5.83	5.76	5.77	5.78	5.77	5.85	5.84
Ti	0.36	0.33	0.35	0.46	0.38	0.46	0.40	0.36
Al	2.48	2.48	2.52	2.59	2.45	2.52	2.40	2.45
Cr	–	–	–	–	–	–	–	–
Fe^{3+}	0.27	0.53	0.51	0.08	0.57	0.36	0.42	0.29
Fe^{2+}	1.40	1.07	1.21	1.34	0.81	0.87	0.88	1.23
Mn	0.03	0.02	0.04	0.01	0.02	0.01	0.01	0.02
Mg	2.60	2.62	2.54	2.78	2.88	2.95	2.94	2.82
Ca	2.00	2.02	2.01	1.98	2.02	2.01	2.01	1.97
Na	0.69	0.70	0.70	0.67	0.63	0.58	0.62	0.68
K	0.20	0.18	0.20	0.24	0.22	0.19	0.21	0.22
X_{Mg}[b]	0.65	0.71	0.68	0.68	0.78	0.77	0.77	0.70

a: bdl: below detection limit.
b: $X_{Mg} = Mg/(Mg + Fe^{2+})$.

Table S6 Bulk rock major and trace element data for the Late Triassic mafic dykes in Eastern Hebei.

No.	J1416	J1501	J1502	J1503	J1504	18NC51	18NC52	18NC53	18NC54	15SHQ03	15SHQ04	15SHQ05	18NC66
Lithology	Gaojiadian dyke					Mataizi dyke				Saheqiao dyke			
Major elements (wt.%)													
SiO_2	47.84	52.44	50.48	49.17	51.32	46.48	49.02	49.81	50.09	45.63	46.76	46.55	47.64
TiO_2	1.86	1.63	1.64	2.85	2.58	1.80	1.71	1.66	1.68	1.80	1.56	1.62	1.74
Al_2O_3	13.25	12.99	13.50	12.57	12.10	12.23	11.54	10.96	11.21	13.67	14.30	14.41	13.37
Fe_2O_{3T}	16.64	14.50	15.35	14.96	14.02	16.84	16.01	15.96	15.79	9.92	10.35	10.49	10.22
MnO	0.22	0.20	0.21	0.19	0.16	0.26	0.23	0.23	0.22	0.17	0.16	0.15	0.15
MgO	6.00	5.19	5.74	5.87	4.44	5.40	5.34	5.35	5.27	8.62	9.21	9.20	7.40
CaO	10.10	8.65	9.39	6.85	6.00	10.05	9.73	9.63	9.11	10.92	9.04	8.82	8.82
Na_2O	2.24	2.18	2.34	2.21	1.80	1.79	1.70	1.62	1.76	3.80	3.42	3.48	4.44
K_2O	0.51	0.47	0.53	1.24	2.11	1.73	1.71	2.04	1.70	0.68	1.47	1.53	1.55
P_2O_5	0.13	0.15	0.12	0.34	0.32	0.16	0.15	0.15	0.15	0.78	0.67	0.68	0.82
LOl	0.22	0.85	0.38	2.92	4.13	2.52	2.07	1.77	2.21	3.45	2.43	2.42	3.13
Total	99.01	99.24	99.69	99.17	98.97	99.25	99.21	99.17	99.19	99.43	99.37	99.36	99.27
Mg#[a]	41.7	41.5	42.6	43.7	38.5	38.8	39.8	39.9	39.8	63.2	63.8	63.5	58.9
Trace elements (ppm)													
Li	15	6	6	14	19	25	21	17	24	11	16	18	37
P	745	780	630	1745	1563	993	1036	1013	1062	3710	3064	3492	5289
K	5222	4258	4351	10724	17416	17724	20120	24440	20860	5598	11540	13334	18954
Sc	53.3	40.1	40.1	27.8	23.8	49.7	50.9	50.5	51.6	32.4	23.2	25.3	29.6
Ti	12882	10400	9801	18036	15036	10440	10558	10614	10956	10458	8870	9666	10846
V	554	413	400	333	284	443	448	443	460	222	184	198	256
Cr	110	89	96	73	63	74	84	81	85	284	369	400	114
Mn	1948	1666	1622	1530	1168	2008	1858	1889	1852	1226	1151	1201	1263
Co	63	53	52	55	46	66	63	62	64	40	44	48	43
Ni	90.1	75.6	81.3	70.7	61.0	53.7	56.5	52.3	56.6	79.1	145.5	156.4	89.6
Cu	287	221	200	92	78	60	95	140	72	74	51	66	99
Zn	131	127	115	114	88	130	132	130	125	64	73	82	115
Ga	24	20	19	23	19	23	22	22	22	17	17	18	22

Rb	16	14	15	33	57	41	46	55	43	8	14	17	20
Sr	158	141	138	309	319	244	237	244	241	2068	1415	1491	2568
Y	32.7	28.2	26.2	27.1	23.0	30.9	30.6	29.4	30.3	23.6	17.8	19.1	26.2
Zr	119	98	93	179	160	98	83	91	93	183	132	142	196
Nb	9.2	8.2	7.6	20.1	17.5	6.4	6.3	6.0	6.2	41.0	32.6	34.8	44.0
Cs	0.50	0.41	0.37	0.73	1.26	0.25	0.22	0.22	0.19	0.24	0.12	0.23	0.26
Ba	137	128	116	448	506	288	301	343	279	486	1226	1538	3627
La	11.6	10.7	9.6	27.0	23.2	12.8	12.7	12.1	12.8	71.3	49.1	51.7	89.0
Ce	26.2	24.5	21.9	58.4	50.6	27.0	26.2	25.5	25.9	148.9	97.1	102.1	163.6
Pr	3.59	3.33	3.00	7.96	6.82	3.93	3.92	3.73	3.88	18.73	11.82	12.58	18.26
Nd	15.6	14.0	12.6	31.1	26.6	16.7	16.6	15.8	16.3	66.3	41.5	44.1	62.4
Sm	4.2	3.7	3.4	6.5	5.6	4.4	4.4	4.2	4.3	10.7	6.8	7.3	10.1
Eu	1.49	1.30	1.21	2.04	1.73	1.39	1.38	1.31	1.33	3.09	2.15	2.30	2.99
Gd	5.1	4.5	4.1	6.3	5.4	5.0	4.9	4.7	4.8	7.9	5.4	5.8	7.5
Tb	0.89	0.78	0.72	0.94	0.80	0.78	0.77	0.73	0.74	0.98	0.70	0.75	0.87
Dy	5.60	4.84	4.51	5.17	4.42	5.02	4.92	4.72	4.72	4.77	3.55	3.78	4.63
Ho	1.19	1.05	0.98	1.03	0.88	1.04	1.02	0.97	0.98	0.89	0.67	0.71	0.85
Er	3.46	2.98	2.78	2.72	2.32	2.84	2.79	2.66	2.68	2.30	1.72	1.84	2.18
Tm	0.50	0.42	0.39	0.36	0.31	0.40	0.40	0.38	0.38	0.30	0.22	0.23	0.29
Yb	3.28	2.63	2.47	2.21	1.89	2.51	2.45	2.35	2.34	1.77	1.31	1.39	1.76
Lu	0.49	0.40	0.38	0.33	0.28	0.32	0.32	0.30	0.30	0.26	0.19	0.20	0.23
Hf	2.80	2.48	2.33	4.29	3.75	2.41	2.06	2.17	2.16	3.72	2.88	3.08	4.40
Ta	0.52	0.46	0.43	1.26	1.13	0.36	0.38	0.37	0.37	2.56	1.86	1.99	2.46
Pb	2.3	2.2	2.2	3.4	3.5	3.5	3.6	3.7	3.6	12.4	8.1	8.1	22.0
Th	1.95	2.19	2.06	3.30	2.94	1.82	1.75	1.67	1.67	8.66	5.36	5.69	9.39
U	0.39	0.46	0.43	0.68	0.59	0.52	0.50	0.47	0.48	3.06	1.67	1.77	2.63
*S*REE	83	75	68	152	131	84	83	79	81	338	222	235	365
Eu/Eu*	0.98	0.98	0.99	0.96	0.95	0.90	0.90	0.90	0.90	0.98	1.05	1.05	1.00
$(La/Yb)_N$[b]	2.5	2.9	2.8	8.8	8.8	3.6	3.7	3.7	3.9	28.9	26.9	26.6	36.3

a: Mg# = molar 100*Mg/(Mg + Fe).
b: Chondrite-normalized; chondrite values are from Sun and McDonough (1989).

Table S7 Bulk-rock Sr-Nd isotopic data for the Late Triassic mafic dykes in Eastern Hebei.

Sample	Rb (ppm)	Sr (ppm)	$^{87}Rb/^{86}Sr$	$^{87}Sr/^{86}Sr$	2SE	$I_{Sr}(t)^a$	Sm (ppm)	Nd (ppm)	$^{147}Sm/^{144}Nd$	$^{143}Nd/^{144}Nd$	2SE	$\varepsilon_{Nd}(0)$	$(^{143}Nd/^{144}Nd)_i^a$	$\varepsilon_{Nd}(t)^a$	T_{DM} (Ma)	$f^{Sm/Nd}$
Gaojiadian dyke																
J1416	16	158	0.283	0.708290	10	0.707348	4.2	15.6	0.170	0.512198	9	-8.6	0.511937	-7.8	1631	-0.14
J1501	14	141	0.279	0.709000	13	0.708072	3.7	14.0	0.168	0.512200	5	-8.5	0.511943	-7.7	1622	-0.15
J1502	15	138	0.312	0.710223	12	0.709471	3.4	12.6	0.169	0.512202	12	-8.5	0.511943	-7.7	1623	-0.14
J1503	33	309	0.298	0.709266	16	0.708275	6.5	31.1	0.133	0.511747	10	-17.4	0.511543	-15.5	2259	-0.32
J1504	57	319	0.504	0.710565	18	0.708887	5.6	26.6	0.133	0.511768	8	-17.0	0.511564	-15.1	2226	-0.32
Mataizi dyke																
18NC51	41	244	0.473	0.708403	6	0.706800	4.4	16.7	0.169	0.512044	8	-11.6	0.511781	-10.7	1870	-0.14
18NC52	46	237	0.549	0.708868	10	0.707010	4.4	16.6	0.168	0.512034	8	-11.8	0.511773	-10.9	1884	-0.15
18NC53	55	244	0.635	0.710812	14	0.708661	4.2	15.8	0.169	0.512042	12	-11.6	0.511779	-10.8	1873	-0.14
18NC54	43	241	0.503	0.708175	10	0.706472	4.3	16.3	0.166	0.512020	8	-12.1	0.511762	-11.1	1902	-0.16
Saheqiao dyke																
15SHQ03	8	2068	0.011	0.704638	9	0.704604	10.7	66.3	0.103	0.512260	6	-7.4	0.512110	-4.7	1381	-0.48
15SHQ04	14	1415	0.028	0.704037	13	0.703948	6.8	41.5	0.104	0.512163	6	-9.3	0.512012	-6.6	1537	-0.47
15SHQ05	17	1491	0.032	0.704704	15	0.704602	7.3	44.1	0.104	0.512165	5	-9.2	0.512013	-6.6	1535	-0.47

Parameters used in the calculation are as follows: ^{87}Rb decay $\lambda = 1.42\times10^{-11}$ year^{-1}; ^{147}Sm decay $\lambda = 6.54\times10^{-12}$ year^{-1}; $(^{147}Sm/^{144}Nd)_{CHUR} = 0.1967$, $(^{143}Nd/^{144}Nd)_{CHUR} = 0.512638$; $(^{147}Sm/^{144}Nd)_{DM} = 0.2137$, $(^{143}Nd/^{144}Nd)_{DM} = 0.51315$.

a: Calculated at zircon U-Pb ages.

Table S8 Bulk rock major element data for rock standards AGV-2, BHVO-2 and GSR-3 and recommended values.

Standard	AGV-2		BHVO		GSR-3	
	Recommended	Average measured (n = 4)	Recommended	Average measured (n = 3)	Recommended	Average measured (n = 4)
wt.%						
SiO_2	59.14	59.13	49.60	49.09	44.64	44.32
TiO_2	1.05	1.06	2.73	2.73	2.36	2.31
Al_2O_3	17.03	17.03	13.44	13.49	13.83	13.79
Fe_2O_{3T}	6.78	6.71	12.39	12.24	13.40	13.03
MnO	0.10	0.11	0.17	0.14	0.16	0.17
MgO	1.80	1.79	7.26	7.68	7.77	7.30
CaO	5.15	5.24	11.40	11.42	8.81	8.73
Na_2O	4.20	4.15	2.22	2.21	3.38	3.41
K_2O	2.90	2.92	0.51	0.54	2.32	2.32
P_2O_5	0.48	0.48	0.27	0.28	0.95	1.00

a: Recommended values for standards are from GeoReM database (http://georem.mpch-mainz.gwdg.de/).

Table S9 Bulk rock trace element data for rock standards AGV-2, W-2 and GSR-3 and recommended values.

Standard	AGV-2		W-2		GSR-3	
	Recommended	Average measured (n = 4)	Recommended	Average measured (n = 3)	Recommended	Average measured (n = 4)
ppm						
Li	10.8	12	9.21	10	10	11
P	2100	2156	611	632	4130	4121
K	23900	23885	5197	5792	19259	19237
Sc	13.11	12.5	35.86	36.6	15	15.0
Ti	6300	6326	6353	6347	14200	14106
V	118.5	120	265.8	268	167	173
Cr	16.22	18	92	93	134	136
Mn	770	824	1293	1314	1310	1333
Co	15.46	17	44.37	45	47	48
Ni	18.87	19.6	72	73.8	140	144.9
Cu	51.51	51	105.9	108	49	49
Zn	86.7	83	77.7	77	150	153
Ga	20.42	20	17.88	18	25	25
Rb	67.79	65	20.23	21	37	37
Sr	659.5	596	195.4	188	1100	1108
Y	19.14	19.4	21.82	22.6	22	22.4
Zr	232	228	93.3	100	277	276
Nb	14.12	15.8	7.51	7.9	68	67.2
Cs	1.173	1.14	0.915	0.98	0.70	0.72
Ba	1134	1162	172.8	174	527	528
La	38.21	37.2	10.63	9.8	56	55.7
Ce	69.43	67.8	23.21	23.1	105	105.2
Pr	8.165	8.32	3.018	2.87	13.2	12.95
Nd	30.49	29.0	13.09	13.0	54	54.7
Sm	5.509	5.7	3.3	3.3	10.2	10.1

Eu	1.553	1.53	1.091	1.05	3.20	3.23
Gd	4.678	4.6	3.713	3.4	8.50	8.5
Tb	0.651	0.66	0.627	0.65	1.20	1.17
Dy	3.549	3.63	3.806	3.62	5.6	5.68
Ho	0.6818	0.67	0.7908	0.77	0.88	0.87
Er	1.825	1.79	2.208	2.50	2.00	1.98
Tm	0.2623	0.26	0.3315	0.39	0.28	0.28
Yb	1.653	1.60	2.054	2.11	1.5	1.53
Lu	0.2507	0.25	0.309	0.33	0.19	0.19
Hf	5.137	5.07	2.444	2.54	6.50	6.60
Ta	0.865	0.88	0.489	0.53	4.30	4.60
Pb	13.14	13.1	7.83	9.4	7	7.1
Th	6.174	6.12	2.179	2.29	6.0	6.02
U	1.885	1.86	0.5048	0.52	1.40	1.40

a: Recommended values for standards are from GeoReM database (http://georem.mpch-mainz.gwdg.de/).